Quantum Intensity Noise Correlation in a Type-II Phase Matched Optical Parametric Oscillator

by

Steven Gregory Patterson

B.S., Electrical and Computer Engineering
University of Cincinnati (1993)

Submitted to the
Department of Electrical Engineering and Computer Science
in partial fulfillment of the requirements for the degree of

Master of Science in Electrical Engineering

at the

MASSACHUSETTS INSTITUTE OF TECHNOLOGY

June 1995

Author.....
Department of Electrical Engineering and Computer Science
May 26,1995

Certified by.....
Dr. N.C. Wong
Research Scientist, Research Laboratory of Electronics
Thesis Supervisor

Accepted by.....
Professor F.R. Morgenthaler
Chairman, Departmental Committee on Graduate Students

Quantum Intensity Noise Correlation in a Type-II Phase Matched Optical Parametric Oscillator

by

Steven Gregory Patterson

Submitted to the Department of Electrical Engineering and Computer Science
on May 26, 1995, in partial fulfillment of the
requirements for the degree of
Master of Science in Electrical Engineering

Abstract

A type-II phase matched optical parametric oscillator is investigated for the generation of intensity correlated twin photon beams using potassium titanyl phosphate (KTP) as a nonlinear medium. The input pump source is a Kr^+-ion laser at $\lambda_p = 531$nm with signal and idler twin photon beams at $\lambda_{s,i} \approx 1.06\mu$m.

Mirror and crystal losses were characterized for use in cavities of two- and three-piece construction. A detection system consisting of two photodetector/transimpedance amplifiers and a summing circuit were developed with a bandwidth of $\approx$40MHz. A feedback stabilization circuit was also implemented to allow locking of the parametric oscillator cavity length to a resonance peak.

The twin beam intensity-difference spectrum of a two-piece optical parametric oscillator was measured yielding 38% correlation (2.1dB) in good agreement with the expected correlation inferred by the loss measurements.

Thesis Supervisor: Dr. N.C.Wong

Title: Research Scientist, Research Laboratory of Electronics

Acknowledgments

I would like to thank Dr. Franco Wong for providing me the opportunity to work on this thesis topic as well as for his guidance, support, and patience. It has been a true pleasure working for someone with his professionalism, motivation, and knowledge. I have learned much and have been enriched by the experience.

Thank you to my parents for teaching me the importance of self-reliance; a quality that has served me well through life.

To two of my undergraduate professors, I'd also like to say thank you. Without the encouragement of Dr. T.D. Mantei it is unlikely I would have ever come to MIT. And in a time where the trend seems to be toward "easier is better," I am grateful to Dr. C. Osterbrock for seemingly believing "easier is rarely better."

To the people with whom I've shared the laboratory my appreciation goes to D. Lee for occasionally lending his superlative experimental skills, E. Mason for always providing a helping hand where needed, and to B. Lai for his assistance in the thesis writing process. In particular I'd like to thank L.R. Brothers for his friendship, humor, conversation, technical skill, and knowledge; each being offered in abundance whenever and wherever needed. Thanks Reg.

Many others have also made MIT an enjoyable experience: J. Ahadian, J. Bounds, D. Carter, A. Duwall, J. Haus, M. Sinn, E. Trias, to name but a few. Thanks guys.

Bob Abrams was a friend indeed during the latter years of my undergraduate days. He was then, and always will be, like a brother to me. Through Glenn Eswein I learned of MIT and at the same time made an enduring, fulfilling friendship. A special thanks goes to my sister Felicia for providing a shoulder to cry on during darker days.

Finally, thanks to Anne for her support and love in the final months of this thesis.

CONTENTS

LIST of FIGURES

List of Tables

CHAPTER 1

INTRODUCTION

Using semiclassical analysis the optical detection of signals is found to be fundamentally limited by the quantized nature of the detection process. In this approach the light is taken to be classical, but the photodetection electrons are taken to be discrete. As a result a minimum noise floor is found to exist; this noise floor is referred to as the shot noise. A more rigorous quantum mechanical analysis, however, shows that the true source of the shot noise is due to the Poisson statistical processes that describe the photon arrival at the detector. This fact is very important in that if the light itself is taken as the source of the shot noise then it is possible to actually achieve sub-shot noise performance by "squeezing" the light. Such states of the optical field have possible application in communications systems, precision measurement and spectroscopy, amongst others.

Previous efforts have used a variety of methods to realize squeezed states including four-wave mixing in atomic vapors and in optical fibers, as well as above and below threshold optical parametric oscillators (OPOs) [1,2]. In the case of an OPO, the cavity was loaded with a nonlinear optical crystal using either type-I or type-II phase matching [1,3,4,5]. The purpose of this work was to construct, characterize, and demonstrate intensity correlation in a type-II phase matched optical parametric oscillator. Additionally, the system was to have the broadest dynamic range and bandwidth achievable, as this would allow for further noise studies in both the parametric amplifier (below threshold) and

parametric oscillator (above threshold) regimes. The optical parametric amplifier/oscillator is attractive for such studies because the nonlinear medium contributes negligible spontaneous emission noise [6].

1.1 BACKGROUND

1.1.1 Quantum Noise

In classical electrodynamics, a complete description of the electromagnetic field can be obtained in accordance with the principles of Hamiltonian mechanics through the measurement of two canonically conjugate variables. In the case of the electromagnetic field an example of canonically conjugate variables would be the two quadratures of the field or, equivalently, the amplitude and phase. A truly complete description of the electromagnetic fields requires the application of quantum mechanics. Quantum mechanically the uncertainty principle applies to any such set of non-commuting observables implying that they cannot be measured with arbitrary accuracy, even in principle. Consequently, quantum mechanics cannot predict precisely the outcome of these measurements but rather must give a probabilistic prediction of the results; some uncertainty must exist. It is worthwhile to point out again that this is not a limitation set by our ability to measure a quantity, since classically no such limit exists, but instead it is an uncertainty imposed by nature as described by the laws of quantum mechanics.

Laser light is of a class known as coherent states [7]. It behaves in the mean as a classical sinusoidal field, and with the two quadratures having equal quantum mechanical uncertainties. Additionally, coherent states are also minimum uncertainty states. A rigorous analysis of the coherent state shows its photons obey Poissonian statistics,

giving rise to the same shot noise as predicted by a semi-classical approach, wherein the light is assumed to be classical but the current carriers in the detector are assumed to be discrete.

If we can prepare or modify the coherent state such that the variance in one variable is diminished (requiring that the uncertainty in the conjugate variable is increased) then the light is said to have been squeezed. This may be visualized by considering two variables, x_1 and x_2, with equal variances, such that when plotted x_1 vs. x_2, the graph is circular. By reducing the variance of x_1, for instance, but increasing that of x_2, then the plot is elliptical, giving the appearance that the original circle has been squeezed [8].

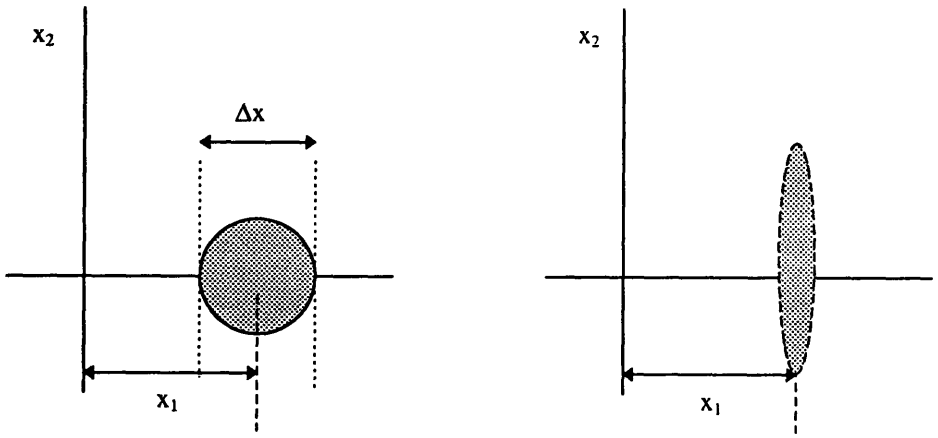

Figure 1.1: "Squeezing" of conjugate variables.

1.1.2 The OPO

Parametric oscillators are best known in electronics. A parameter in a resonant circuit is varied such that if the variation is done at the correct frequency with the correct phase, energy is added to the system [9,10]. For instance, by varying the capacitance of an RLC

circuit at twice the natural frequency of the circuit (with the correct phase) more and more energy may be stored in the resonator (which is resonating at the natural frequency). By analogy we can consider:

$$P(t) = \varepsilon_0 \chi E(t) + d_{eff} E^2(t) \qquad (1.1)$$

$$D(t) = \varepsilon_0 E(t) + P(t) = \varepsilon E(t) \qquad (1.2)$$

$$\varepsilon = \varepsilon_0 (1 + \chi) + d_{eff} E(t) \qquad (1.3)$$

Here the factor d_{eff} in equations (1.1) and (1.3) represents the effective interaction between the nonlinear crystal and the applied electric field . This factor is a function of the material properties and the angle of incidence of the **E** field. By solving Maxwell's equations it can be shown that a "pump" field at ω_p can generate frequencies at ω_s and ω_i such that $\omega_p = \omega_s + \omega_i$[11]. Multiplying this equation by $\hbar$ yields the quantum mechanical expression for conservation of energy. A nonlinear medium that can produce such an interaction is referred to as a $\chi^{(2)}$ medium. The two resulting frequencies, ω_s and ω_i are known as the signal and idler frequencies, respectively. There is no convention as to which is called the signal and which the idler. In the experiment to be described later, the $\chi^{(2)}$ medium is KTP (potassium titanyl phosphate, used for its strong nonlinear properties), the pump is a krypton-ion laser with $\lambda_p = 531$ nm and the signal and idler beams nearly degenerate with $\lambda \approx 1.06$ μm. A more rigorous description of the OPO and its use as a source of squeezed light will be provided in subsequent chapters, but for now it is useful to see the analogy between the circuit description of a parametric interaction and the case of an OPO where a strong pump provides energy to oscillations at half the pump frequency.

The slowly varying envelope approximation uses a nonlinear, but still classical, approximation to Maxwell's equations. This approach is advantageous in describing nonlinear interactions and can be shown to be equivalent to a full quantum mechanical

formulation of the interaction [6]. When each pump photon is destroyed in the nonlinear interaction two photons, one signal and one idler, are simultaneously created (this process is known as spontaneous parametric down conversion). These photon beams are said to be well correlated since if separated and then detected, the signal and idler photocurrents generated will have identical shot noise signatures. Obviously, if any photon is destroyed before detection, there will be a reduction in the intensity correlation of the two beams. The cavity surrounding the nonlinear crystal does introduce some decorrelation as we cannot be completely certain that each member of the down-converted photon pair escapes the cavity at the same time, but if the observation time is much greater than the characteristic decay time of the cavity (i.e. the inverse of the cavity linewidth) then, statistically speaking, we can say both photons have indeed exited the cavity. Stated another way, we expect to see significant squeezing only at frequencies less than the cavity bandwidth.

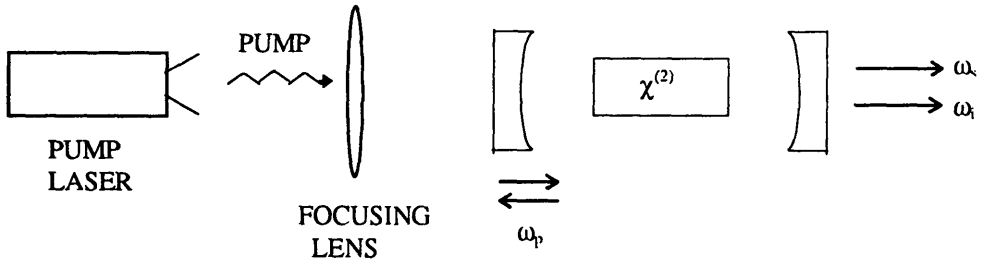

Figure 1.2: The optical parametric oscillator.

1.2 Intensity Correlation

We define a field loss parameter κ, as the total loss rate in the cavity, such that [12]:

$$\kappa = \gamma + \mu \qquad (1.4)$$

where γ and μ represent losses due to the output coupling of the signal (or idler), and losses due to all other causes in the cavity (assumed equal for both the signal and idler in both cases), respectively.

Then the low-frequency noise density of the OPO intensity correlation is given by [2]:

$$S_{OPO} = \frac{\gamma}{\kappa} = 1 - \frac{\gamma}{\kappa} \tag{1.5}$$

Note that if μ is zero, $S_{OPO} = 0$, implying perfect correlation between the intensities of the signal and idler outputs.

We can now say that:

$$S_{DETECTED} = S_{OPO}\eta + (1 - \eta)\, S_{VAC} \tag{1.6}$$

where $\eta = \eta_{DET} * \eta_{PROP} * \eta ...$ is the external detection efficiency, and $S_{VAC} = 1$ is the vacuum shot noise level.

Hence:

$$S_{DETECTED} = 1 - \frac{\eta\gamma}{\kappa} \tag{1.7}$$

We may now define the amount of squeezing as:

$$\text{Amount of Squeezing} \equiv S_{VAC} - S_{DETECTED} = \frac{\eta\gamma}{\kappa} = \frac{\eta\gamma}{\gamma + \mu} \tag{1.8}$$

By examining this equation we realize that the amount of observable squeezing may be increased by:

- increasing η
- increasing γ (relative to the internal loss)
- decreasing μ relative to γ

This result is intuitively pleasing. A less than ideal ($\eta < 1$) detection system can be viewed as a partially transmitting beamsplitter plus an ideal photodetector. The beamsplitter randomly deletes incoming photons and hence reduces the intensity correlation of the OPO. Therefore, it is important to have a high detection quantum efficiency. Likewise, the greater γ, the greater the probability the photons will be coupled out of the cavity (together) and again the better the intensity correlation. Finally, decreasing μ reduces the number of photons destroyed, since loss is a random photon depletion process, with a resultant increase in correlation. It is worthwhile to point out that increasing γ also increases κ so that, for instance, doubling γ does not double the amount of squeezing for $\mu \neq 0$.

1.3 Experimental Considerations

Aside from minimizing cavity and detection losses as indicated in the previous section several other points of concern needed to be addressed in order to design a functioning parametric amplifier/oscillator system. In this experiment a double pass pump was used, i.e. it couples into the cavity through the front mirror, passes through the crystal, reflects from the back mirror, passes a second time through the crystal, and exits the cavity through the front mirror. This double pass configuration has the effect of reducing the threshold power by a factor of 2 to 4[13]. Additionally, both the signal and idler beams will be resonant in the cavity; this is referred to as a DRO or Doubly Resonant OPO.

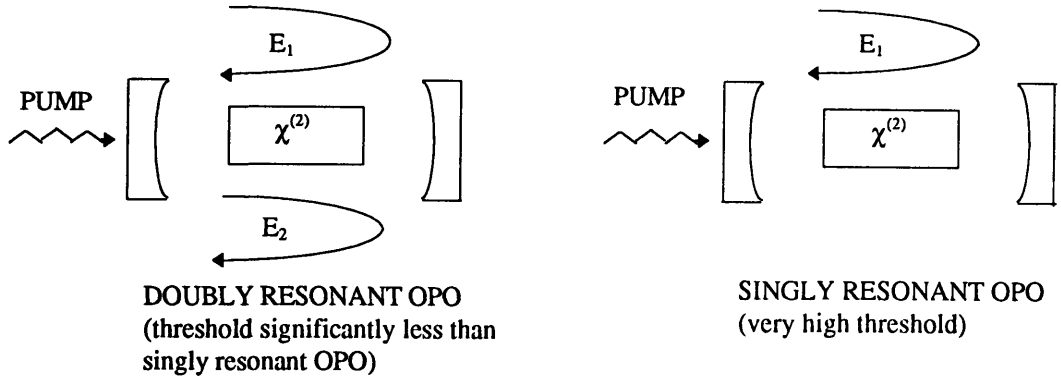

Figure 1.3: Doubly and singly resonant optical parametric oscillators.

Another point of interest is the walk-off exhibited in anisotropic media. When the components of an E-field lie along crystal axes with different indices of refraction, the directions of the phase velocity and energy propagation are not collinear. The result is a reduction in the distance over which the nonlinear interaction takes place. It has been shown by Boyd and Kleinman [14] that such walk-off for focused Gaussian beams reduces the conversion efficiency (as well as possibly the intensity correlation). This point will be addressed in two ways. First, by increasing the beam size in the cavity this effect can be diminished. Physically this makes sense since beams of large diameter will overlap over greater distances for any given amount of walk-off. Another technique that was tried involved a specially cut crystal to reduce the effect of walk-off and has been used in one design of an internally doubled YAG laser that uses KTP as the second-harmonic generation crystal [15].

There were three possibilities for the cavity design. One was a monolithic cavity with the mirror surfaces formed onto the crystal itself. Although it has the lowest cavity losses of the three designs, many practical difficulties rendered this option intractable. Two- and three-piece designs are more flexible, providing greatly simplified alignment and tuning, but at the expense of increased losses and inherent cavity instability. These facets will be discussed in greater detail in Chapter 4.

It is necessary to intensity- and frequency-lock the krypton-ion laser as these parameters fluctuate strongly. This has been determined to be caused primarily, in earlier work, by the excitation of the resonant mechanical structure of the laser cavity induced by the flowing cooling water [16,17]. These problems have been adequately addressed in earlier work and warrant mention here as points of experimental concern.

This mechanical noise, as mentioned previously, also affects the stability of the OPO. To suppress this vibrational effect a feedback loop is employed where the DC signals from the two photodetectors are summed and compared to a quiet, stable DC reference. The feedback DC signal is the sum of the DC signals from the two photodetectors, and hence proportional to the intensity of the twin beams. The output of this system is then integrated (the 1/s frequency response allows high gain to suppress the low frequency noise but rolls off quickly at higher frequencies, where the mechanical noise is less of a problem, allowing system stability) and fed back to the cavity via a PZT drive that controls the cavity length.

1.4 Thesis Organization

This thesis describes the characterization, design, and testing of an optical parametric oscillator with attendant detection and stabilization circuitry used to generate intensity-correlated twin photon beams. Chapter 2 provides the necessary theory to understand the generation of parametrically down-converted photons via nonlinear interactions in a crystal. Chapter 3 presents the theory of the intensity correlation of the photon pairs generated by this nonlinear interaction. Chapter 4 describes the experimental techniques and set-up used, as well as the results of the experiment performed. The concluding chapter summarizes the thesis contents as well as presenting suggested directions for future work.

CHAPTER 2

NONLINEAR WAVE INTERACTIONS AND PARAMETRIC OSCILLATION

This chapter puts the nonlinear processes described in the previous chapter on a firmer theoretical footing. In section 2.1, through suitable approximation, a set of coupled wave equations is derived from Maxwell's equations. When solved using appropriate boundary conditions these equations yield a variety of nonlinear interactions. The particular interaction of interest, a parametric oscillator, will be solved in section 2.2. In section 2.3 a set of energy conservation equations, known as the Manley-Rowe relations, will be derived coupling the wave picture to the photon picture. Topics of interest that occur along the way, the concepts of the d_{eff} term and phase-matching, will be addressed in sections 2.4 and 2.5, respectively. Throughout, the developments of this chapter follow closely those given in reference [11].

2.1 Maxwell's Equations and Nonlinear Interactions

Maxwell's equations in mks units appear as follows:

$$\nabla \times \mathbf{E} = -\frac{\partial \mathbf{B}}{\partial t} \tag{2.1a}$$

$$\nabla \times \mathbf{H} = \frac{\partial \mathbf{D}}{\partial t} + \mathbf{J} \tag{2.1b}$$

$$\nabla \cdot \mathbf{D} = \rho \tag{2.1c}$$

$$\nabla \cdot \mathbf{B} = 0 \tag{2.1d}$$

With the constitutive relationships:

$$\mathbf{D} = \varepsilon \mathbf{E} = \varepsilon_o (1 + \chi)\mathbf{E} = \varepsilon_o \mathbf{E} + \mathbf{P} \tag{2.2a}$$

$$\mathbf{B} = \mu \mathbf{H} \tag{2.2b}$$

$$\mathbf{J} = \sigma \mathbf{E} \tag{2.2c}$$

where in general ε, μ, σ and χ are tensors.

The simplest picture of an electromagnetic (EM) field interacting with an atom consists of an electron being pulled away from the nucleus by the force generated from the E-field's interaction with the charged electron. The polarization term **P** (or equivalently $\varepsilon_o \chi \mathbf{E}$) in equation (2.2a) results from this interaction. This force is oppositely directed to that of the (assumed to be linear) restoring force provided by the nucleus. Solution of the classical equations would yield simple harmonic motion resulting in reradiation at the same frequency as the driving field. If the electric field is quite strong, as might be generated by a laser, then the excursions of the electrons from their equilibrium positions would be comparably large, and the restoring force could no longer be considered linear. In this case one would expand the polarization term as a power series in **E**:

$$\mathbf{P} = \varepsilon_o(\chi^{(1)} + \chi^{(2)}\mathbf{E} + \text{higher order terms})\mathbf{E} \tag{2.3}$$

The first term in this expansion is linear and gives rise to the commonly known dielectric constant. It is the second term that is of interest in the process of down-conversion. Higher order terms are, of course, always present but significantly weaker than the second order term of interest. Hence, we may define a nonlinear polarization term that will shortly be shown to be the driving term for the nonlinear interaction:

$$\mathbf{P}_{NLi} = \hat{p}_i \varepsilon_o \sum \chi_{ijk} E_j E_k \tag{2.4}$$

In practice the χ tensor is replaced by a quantity d_{eff} (see section 2.5).

Proceeding in the normal manner for the development of the wave equation and taking the curl of equation (2.1a):

$$\nabla \times \nabla \times \mathbf{E} = -\mu o \frac{\partial \nabla \times \mathbf{H}}{\partial t} \tag{2.5}$$

Using the vector identity $\nabla \times \nabla \times \mathbf{E} = \nabla(\nabla \cdot \mathbf{E}) - \nabla^2 \mathbf{E}$ and substituting equation (2.1b) yields:

$$\nabla(\nabla \cdot \mathbf{E}) - \nabla^2 \mathbf{E} = -\mu_o \frac{\partial^2 \mathbf{D}}{\partial t^2} - \mu_o \sigma \frac{\partial \mathbf{E}}{\partial t} \tag{2.6}$$

Taking $\nabla \cdot \mathbf{E} = 0$, and introducing the nonlinear term $\mathbf{D} = \varepsilon E + \mathbf{P}_{NL}$ results in:

$$\nabla^2\mathbf{E} - \mu_o\varepsilon\frac{\partial^2\mathbf{E}}{\partial t^2} - \mu_o\sigma\frac{\partial\mathbf{E}}{\partial t} = \mu_o\frac{\partial^2\mathbf{P}_{NL}}{\partial t^2} \qquad (2.7)$$

where each component of $\mathbf{P}_{NL}$ is given by equation 2.4.

In the most general (tensor) case, this equation is quite difficult to solve. With suitable approximation, a useful result is obtained, while retaining the essential physics. We assume non-tensor quantities and a slowly varying envelope solution of the form:

$$\mathbf{E}(z,\omega,t) = \hat{\mathbf{e}}\ \mathbf{E}(z,t)\,e^{-j(kz-\omega t)} \qquad (2.8)$$

where $\mathbf{E}(z,t)$ is the slowly varying envelope.

Substitution of this approximation into equation (2.7) yields:

$$\left[\frac{\partial^2}{\partial z^2} - 2jk\frac{\partial}{\partial z} - k^2 - \mu_o\sigma\left(\frac{\partial}{\partial t} + j\omega\right) - \mu_o\varepsilon\left(\frac{\partial^2}{\partial t^2} + 2j\omega\frac{\partial}{\partial t} - \omega^2\right)\right]E(z,t)e^{-j(kz-\omega t)}$$

$$= \mu_o\left(\frac{\partial^2}{\partial t^2} + 2j\omega\frac{\partial}{\partial t} - \omega^2\right)\hat{\mathbf{e}}\cdot\hat{\mathbf{p}}\,P_{NL}e^{-j(k_p z-\omega t)} \qquad (2.9)$$

Recalling the dispersion relationship $k^2 = \mu_o\varepsilon\omega^2$ and making the further approximations that:

$$k\frac{\partial E}{\partial z} >> \frac{\partial^2 E}{\partial z^2} \qquad (\Delta E \text{ negligible for } \Delta z < \lambda) \qquad (2.10)$$

$$\omega\frac{\partial E}{\partial t} >> \frac{\partial^2 E}{\partial t^2} \qquad (\Delta E \text{ negligible for } \Delta t < \omega^{-1})$$

$$\omega^2 P >> \omega\frac{\partial P}{\partial t} >> \frac{\partial^2 P}{\partial t^2}$$

equation (2.9) becomes:

$$\left[-2jk\frac{\partial}{\partial z} - k^2 - j\omega\mu_o\sigma - 2j\omega\mu_o\varepsilon\frac{\partial}{\partial t})\right]E(z,t)e^{-j(kz-\omega t)}$$

$$= -\mu_o\omega^2\,(\hat{\mathbf{e}}\cdot\hat{\mathbf{p}})\,P_{NL}e^{-j(k_p z-\omega t)} \qquad (2.11)$$

Using the relationship $\frac{\omega}{k} = \frac{c}{n}$ a loss parameter $\kappa = \frac{\mu_o\sigma c}{2n}$ may be defined further reducing equation (2.11) to its final form:

$$\left[\frac{\partial}{\partial z} + \kappa - \frac{n}{c}\frac{\partial}{\partial t}\right]E(z,t) = \frac{-j\omega\mu_o c}{2n}(\hat{\mathbf{e}}\cdot\hat{\mathbf{p}})\,P_{NL}\,e^{j(k-k_p)z} \qquad (2.12)$$

An equation of this form would appear for each wave in the interaction.

2.2 The Optical Parametric Oscillator

As previously mentioned we may write the second order nonlinear term as:

$$P_i(\omega_i) = \varepsilon_o \sum_{j,k} d_{ijk}(\omega_i : \omega_m, \omega_n)\, E_j(\omega_m) E_k(\omega_n)$$

where i, j, k may take on the coordinate directions x, y, and z and l, m, n may take on the values p, s, and i (for pump, signal, and idler, respectively). In order to greatly simplify matters, the summation over crystal indices given above is replaced by a quantity d_{eff} for a coordinate system defined by the wave in the crystal (see section 2.4). The d coefficients are equal in each of the three equations describing the interaction as required by energy conservation. If we also assume, for simplicity, that **E** and **P** are parallel we then arrive at the following set of coupled equations as derived in equation (2.12):

$$\frac{\partial E(w_s)}{\partial z} + \kappa_s E(w_s) = -j\frac{\omega_s d_{eff}}{n_s c} E(\omega_p) E^*(\omega_i) e^{-j\Delta k z} \qquad (2.13a)$$

$$\frac{\partial E(\omega_i)}{\partial z} + \kappa_i E(\omega_i) = -j\frac{\omega_i d_{eff}}{n_i c} E(\omega_p) E^*(\omega_s) e^{-j\Delta k z} \qquad (2.13b)$$

$$\frac{\partial E(\omega_p)}{\partial z} + \kappa_p E(\omega_p) = -j\frac{\omega_p d_{eff}}{n_p c} E(\omega_s) E(\omega_i) e^{j\Delta k z} \qquad (2.13c)$$

where $\Delta k = k_p - k_s - k_i$.

Assuming an undepleted pump ($E(\omega_p)$ = constant) and solutions of the form $E(\omega) \propto e^{g'z - j\Delta k z/2}$ equations (2.13) become:

$$\left[g' + \kappa_s - \frac{j\Delta k}{2}\right] E(\omega_s) + \left[\frac{j\omega_s d_{eff}}{n_s} E(\omega_p)\right] E^*(\omega_i) = 0 \qquad (2.14a)$$

$$-\left[\frac{j\omega_i d_{eff}}{n_i}E^*(\omega_p)\right]E^*(\omega_s)+\left[g'+\kappa_i-\frac{j\Delta k}{2}\right]E(\omega_i)=0 \qquad (2.14b)$$

with the determinant of coefficients yielding the relationship:

$$g'=-\frac{(\kappa_s+\kappa_i)}{2}\pm\sqrt{\left\{\left[\frac{(\kappa_s-\kappa_i)}{2}+\frac{j\Delta k}{2}\right]^2+\frac{\omega_s\omega_i d^2_{eff}}{n_s n_i}|E(\omega_p)|^2\right\}} \qquad (2.15)$$

and defining for future use:

$$g^2=\frac{\omega_s\omega_i d^2_{eff}}{n_s n_i c^2}|E(\omega_p)|^2 \qquad (2.16)$$

It can be clearly seen from this equation the importance of keeping the losses ($\kappa_{s,i}$), and phase-mismatch (Δk) small. Placing a cavity around the crystal such that the pump makes a single pass through the cavity (both mirrors are high transmitters at the pump wavelength) but the signal and idler make double passes (both mirrors are high reflectors at the signal and idler wavelengths) creates the condition necessary to establish a low threshold (doubly resonant) oscillation. If we do assume Δk to be zero (something that is, in practice, possible or nearly possible) but non-zero values for the single pass loss coefficient, $\kappa_{s,i}$, we get solutions that look as follows:

$$E(\omega_s,l)e^{\kappa_s l}=E_o(\omega_s)\cosh gl-j\frac{\omega_s d_{eff}}{gn_s c}E(\omega_p)E_o^*(\omega_i)\sinh gl$$

$$E(\omega_i,l)e^{\kappa_i l}=E_o(\omega_i)\cosh gl-j\frac{\omega_i d_{eff}}{gn_i c}E(\omega_p)E_o^*(\omega_s)\sinh gl$$

Making the approximation $e^{2\kappa l} \cong 1 + 2\kappa l$ and solving for the determinant of coefficients gives the following relationship:

$$\cosh gl = 1 + \frac{2\kappa_s \kappa_i l^2}{1 - \kappa_s l - \kappa_i l} \tag{2.17}$$

or for small losses:

$$(gl)^2 \cong (2\kappa_s l)(2\kappa_i l) \tag{2.18}$$

It is necessary to point out that the parameter κ is an effective loss parameter and represents losses due to all causes. In the experimental work to be described later the losses due to reflections at interfaces, absorption, transmission, etc. were characterized to ensure they resided within acceptable ranges. If, however, one or both of the signal and idler waves are not at or near resonance the losses would be very large compared to other causes, raising the threshold by orders of magnitude. Since the signal and idler "see" different effective cavity lengths (due to the different index of refraction for the ordinary and extraordinary waves) the mode spacings differ, yielding only a discrete set of modes, or mode clusters, at which the requirements of energy and momentum conservation are met.

To further minimize the oscillation threshold the pump was operated double pass. This has been shown to reduce the oscillation threshold by a maximum of $(1+R_p)^2$, where R_p is the reflectivity of the pump intensity at the back mirror [13]. The exact value depends upon the relative phase shifts experienced by each of the three waves upon reflection from the mirror. For R_p approximately equal to one a reduction factor as high as four is therefore possible.

2.3 The Manley-Rowe Relations

Returning to equation (2.13a) and multiplying by $\frac{n_s c\varepsilon_o E^*(\omega_s)}{2\omega_s}$, then adding this to its complex conjugate we get:

$$\left(\frac{1}{\omega_s}\right)\frac{dI(\omega_s)}{dz} = j\frac{\varepsilon_o d_{eff}}{2}E(\omega_p)E^*(\omega_s)E^*(\omega_i)e^{-j\Delta kz} + c.c. \qquad (2.19)$$

Repeating these operations on equation (2.13b) yield the same left side with the indices replaced by i, and the same right side. The same operations on (2.13c) give, again, the same right side but with the left side opposite in sign (with the appropriate indice change as well). Setting all three left sides equal and dividing through by $\hbar$ gives:

$$\left(\frac{1}{\hbar\omega_s}\right)\frac{dI(\omega_s)}{dz} = \left(\frac{1}{\hbar\omega_i}\right)\frac{dI(\omega_i)}{dz} = -\left(\frac{1}{\hbar\omega_p}\right)\frac{dI(\omega_p)}{dz} \qquad (2.20)$$

This is a conservation of energy equation stating that for each photon destroyed at ω_p one photon must be created at ω_s and one at ω_i. This couples the classical wave picture to the quantum mechanical photon picture.

2.4 The d_{eff} Tensor

In tensor form the equation:

$$P_i(\omega_1) = \varepsilon_o \sum_{j,k} d_{ijk}(\omega_1 : \omega_m, \omega_n)\, E_j(\omega_m)E_k(\omega_n) \qquad (2.21)$$

is written:

$$\begin{bmatrix} P_x \\ P_y \\ P_z \end{bmatrix} = \varepsilon_o \begin{bmatrix} d_{11} & d_{12} & d_{13} & d_{14} & d_{15} & d_{16} \\ d_{21} & d_{22} & d_{23} & d_{24} & d_{25} & d_{26} \\ d_{31} & d_{32} & d_{33} & d_{34} & d_{35} & d_{36} \end{bmatrix} \begin{bmatrix} E_x^2 \\ E_y^2 \\ E_z^2 \\ 2E_yE_z \\ 2E_xE_z \\ 2E_xE_y \end{bmatrix} \qquad (2.22)$$

Due to a variety of symmetry properties some of these coefficients may be zero, equal in magnitude but opposite in sign, or equal both in magnitude and sign. The type of crystal used in this experiment, potassium titanyl phosphate or KTP ($KTiOPO_4$), has an orthorhombic unit cell and belongs to point group mm2. As a result the only non-zero d coefficients are d_{31}, d_{32}, d_{33}, d_{24}, and d_{15}.

We define a unitary transformation tensor [18]:

$$\overline{\overline{T}} = \begin{pmatrix} \sin\phi & -\cos\phi & 0 \\ \cos\theta\cos\phi & \cos\theta\sin\phi & -\sin\theta \\ \sin\theta\cos\phi & \sin\theta\sin\phi & \cos\theta \end{pmatrix} \qquad (2.23)$$

where θ is the angle made between the k-vector and the z-axis of the crystal, and ϕ is the angle between the E-vector laying in the x-y plane and the x-axis.

Equation (2.21) may now be written as:

$$P_\alpha = \overline{\overline{T}}_{\alpha i} P_i = \varepsilon_o \overline{\overline{T}}_{\alpha i} d_{ijk} \overline{\overline{T}}^{-1}_{j\beta} \overline{\overline{T}}_{\beta l} E_l \overline{\overline{T}}^{-1}_{k\gamma} \overline{\overline{T}}_{\gamma m} E_m = \varepsilon_o \overline{\overline{T}}_{\alpha i} d_{ijk} \overline{\overline{T}}^{-1}_{j\beta} \overline{\overline{T}}^{-1}_{k\gamma} E_\beta E_\gamma \quad (2.24)$$

where the Einstein convention of summation over repeated indices is assumed , $\overline{\overline{T}}^{-1}$ is given by the transpose of equation (2.23), and P_α, E_β, and E_γ are the component polarization and electric fields in the coordinate system defined by the fields. We may then identify:

$$d_{eff} = \varepsilon_o \overline{\overline{T}}_{\alpha i} d_{ijk} \overline{\overline{T}}^{-1}_{j\beta} \overline{\overline{T}}^{-1}_{k\gamma} = (d_{24} - d_{15}) \sin 2\theta \sin 2\phi - (d_{15} \sin^2\phi + d_{24} \cos^2\phi) \sin\theta \quad (2.25)$$

for a type-II phase matched KTP crystal.

2.5 Phase Matching

As was previously mentioned, for best amplification, a phase matching condition must be met such that:

$$\mathbf{k}_p = \mathbf{k}_s + \mathbf{k}_i$$

Multiplying this equation by $\hbar$ one finds the quantum mechanical expression for conservation of momentum. Assuming co-linear k-vectors this reduces to:

$$\frac{n_p}{\lambda_p} = \frac{n_s}{\lambda_s} + \frac{n_i}{\lambda_i} \quad (2.26)$$

The indices of refraction of the three crystallographic axes are, in general, functions of wavelength. The dependence of n_x, n_y, and n_z on λ is given by the Sellmeier equations (see section 4.1).

We define a tensor:

$$\left(\frac{1}{n^2}\right)=\begin{pmatrix}\frac{1}{n_x^2} & 0 & 0\\ 0 & \frac{1}{n_y^2} & 0\\ 0 & 0 & \frac{1}{n_z^2}\end{pmatrix} \tag{2.27}$$

for the crystallographic coordinate system. This can be transformed into the system defined by the fields in the crystal through the use of equation (2.23):

$$\left(\frac{1}{n^2}\right)'(\theta,\phi)=\overline{\overline{T}}\bullet\left(\frac{1}{n^2}\right)\bullet\overline{\overline{T}}^{-1} \tag{2.28}$$

and where:

$$\mathbf{E}'=\frac{1}{\varepsilon_o}\left(\frac{1}{n^2}\right)'\bullet\mathbf{D}'=\frac{1}{\varepsilon_o}\overline{\overline{T}}\bullet\left(\frac{1}{n^2}\right)\bullet\overline{\overline{T}}^{-1}\overline{\overline{T}}\bullet\mathbf{D} \tag{2.29}$$

where primed quantities denote the field-defined coordinate system.

Using equations (2.26), (2.28), and (2.29), with the elements of equation (2.27) given by the Sellmeier equations, and solving Maxwell's equations in the kDB system as defined in [18], one may find the correct phase matching angles. For this experiment the phase matching condition was met with the pump k-vector and E-vector both residing in the x-y plane ($\theta = 90°$) propagating at an angle of 23.18° with respect to the x-axis. The crystal was cut such that the crystal normal met this requirement.

Graphically this appears as (for the degenerate case):

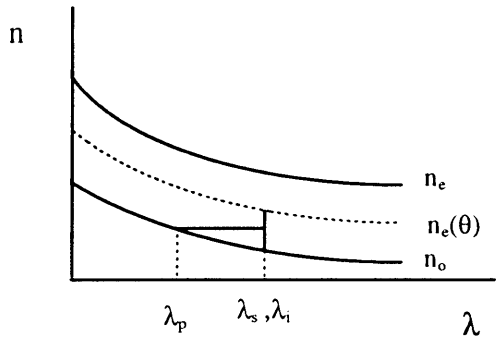

Figure 2.1. Graphical representation of type-II phase matching in the degenerate case.

CHAPTER 3

NOISE AND THE INTENSITY CORRELATION SPECTRUM

In this chapter we investigate the primary sources of noise of interest in Chapter 4 as well as the expected output noise spectrum of the OPO, to include, at least qualitatively, certain non-idealities. In section 3.1 the issue of shot noise is addressed along with its relationship to the output of a single mode laser, as described quantum mechanically by what is termed the coherent state. Also in this section the equation for thermal noise in a resistor is formulated. In section 3.2 the OPO output spectrum is derived for the simplest case of balanced channels with resonant signal and idler. Additionally, non-idealities such as unbalanced channels, detuning, and pump noise are discussed. The presentation parallels that of reference [19].

3.1 Shot and Thermal Noise

If one were to illuminate a photodiode in a transimpedance configuration with laser light and observe the output spectrum one would find, over most observable frequencies, a flat output spectrum of a particular magnitude.

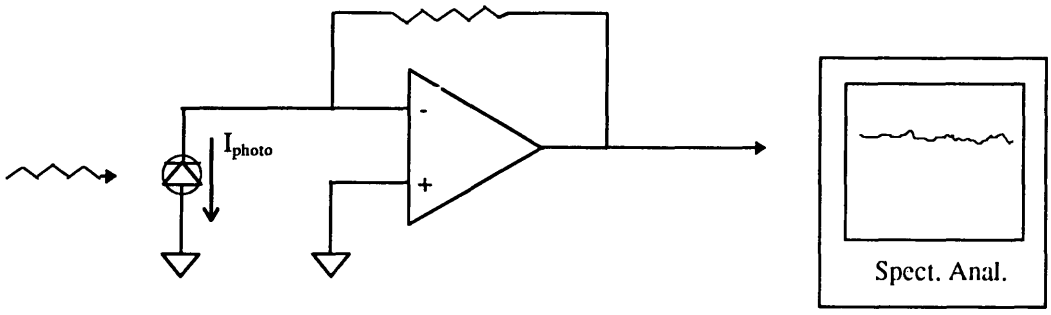

Figure 3.1: Shot noise induced by photodetection.

If the photodiode were now replaced with a resistor equivalent to the junction resistance of the photodiode, and the circuit were driven at a current equivalent to that provided by the photocurrent, a similar flat spectrum would be found, but with reduced power; the difference being proportional to the DC photocurrent. For this reason shot-noise was originally assumed to originate from the quantized nature of the carriers in the photodetector. As we'll shortly see, this is not the case.

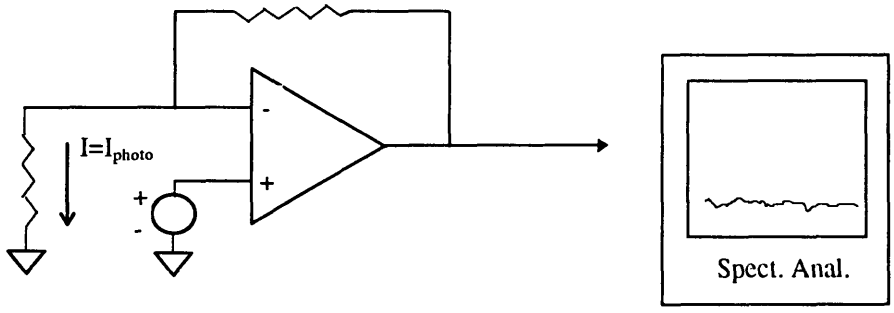

Figure 3.2: Noise of equivalent circuit driven at $I = I_{photo}$.

Turning our attention to the light field it is found that a single mode EM field may be written as a superposition of quantum mechanical harmonic oscillator wave functions [8]:

$$\Psi = \sum_n c_n e^{-i\omega(n+\frac{1}{2})t} |n\rangle \tag{3.1}$$

where:

$$|n\rangle = A e^{\frac{x^2}{x_0^2}} H_n(x)$$

with A a normalization constant and $H_n(x)$ being the Hermite polynomials.

With the choice of :

$$c_n = \left(\frac{e^{-\langle n \rangle} \langle n \rangle^n}{n!} \right)^{\frac{1}{2}} e^{-in\varphi} \tag{3.2}$$

this superposition takes on interesting properties. The first of these comes from the variance of the position variable. By taking the inner products $\langle \Psi | \hat{x} | \Psi \rangle$ and $\langle \Psi | \hat{x}^2 | \Psi \rangle$, replacing the position operators with the appropriate raising and lowering operators, using the orthoginality of the Hermite polynomials, and then applying the definition of the variance ($\Delta x^2 = \langle x^2 \rangle - \langle x \rangle^2$) we find:

$$\Delta x^2 = L^2/2$$

and similarly for the momentum variable:

$$\Delta p^2 = \hbar^2/2L^2$$

where $L \equiv \left(\frac{M\omega}{\hbar} \right)^{\frac{1}{2}}$ and M is the "mass".

This gives the uncertainty product:

$$(\Delta x)^2 (\Delta p)^2 = \frac{\hbar^2}{4}$$

So with this choice of coefficients we create a time-independent minimum uncertainty state, which is necessarily Gaussian with a phase that is linear in x. If one were to carry out a similar procedure to determine the mean and variance for the number of energy quanta in the mode, it would be found that they are both equal to $\langle n \rangle$ as given in equation (3.1). Statistical distributions with equivalent means and variances are said to be Poisson distributed. Laser light is of the form given by equation (3.1) with coefficients as given by equation (3.2). This is the closest quantum-mechanical description there is to a classically oscillating field. As will be shown shortly, it is this Poisson statistical property of the laser field that is actually responsible for shot-noise.

An observation of extreme importance is that even with zero mean field (i.e. $\langle n \rangle = 0$) a coherent state exists; $|\Psi\rangle = |0\rangle$. These ground state fluctuations are the origin of vacuum noise and can be coupled in to a cavity through all open ports.

The DC photocurrent generated by the laser light is given by:

$$I_{DC} = \frac{e}{T}\langle n \rangle \qquad (3.3)$$

where e is the charge per electron-hole pair generated by an expected number of photons $\langle n \rangle$ in a time period T. The mean square fluctuation would then be given as:

$$\langle \Delta i^2 \rangle = \left(\frac{e}{T}\right)^2 \langle \Delta n^2 \rangle = \left(\frac{e}{T}\right)^2 \langle n \rangle = \left(\frac{e}{T}\right)^2 \frac{T}{e} I_{DC} = \left(\frac{e}{T}\right) I_{DC} \qquad (3.4)$$

using the properties of a Poisson distribution and equations (3.2) and (3.3). If we assume $T = \frac{1}{2\Delta f}$ (counting both negative and positive frequency contributions) this further reduces to:

$$\bar{i}_{SN}^2 = \langle \Delta i^2 \rangle = 2eI_{DC}\,\Delta f \qquad (3.5)$$

where Δf is the resolution bandwidth of the spectrum analyzer. In this way we see that it is the Poisson distribution inherent in the laser field that gives rise to the shot noise, since without the presence of a second moment, the shot noise would be zero. It is imperative to note that although the source of the shot noise is DC, the shot noise itself is purely AC.

Another source of noise that will appear in the subsequent chapter is that due to thermal, or Johnson noise. The simplest model is one of a transmission line of characteristic impedance Z_o loaded on either end by resistors of value $R = Z_o$, which implies no reflections [9]. The source of the noise is due to the random thermal motion of the carriers in the resistors, which introduce momentary charge gradients, in turn sourcing alternating voltage fluctuations.

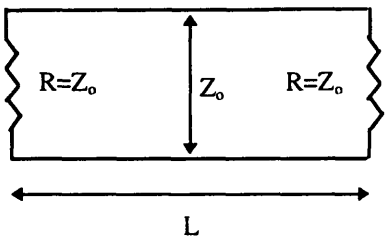

Figure 3.3: Transmission line model for the determination of resistor thermal noise.

If the requirement is imposed for periodic boundary conditions then the restriction placed upon the allowed k values is:

$$k = \frac{2\pi m}{L} \quad \text{for m a non-zero positive integer}$$

This restriction further implies the following:

$$\Delta k = \frac{2\pi}{L} \quad \text{(mode spacing)}$$

$$N_k = \frac{kL}{2\pi} = \frac{f\,L}{c} \quad \text{(number of modes in the interval from zero to k)}$$

$$\rho(f) = \frac{dN_k}{df} = \frac{L}{c} \quad \text{(number of modes per unit frequency)}$$

Using these relations and Planck's Law for the energy per mode $= \dfrac{\hbar\omega}{e^{\frac{\hbar\omega}{kT}} - 1}$ gives the power:

$$P = \left(\frac{\text{energy / mode} \times \text{ number of modes between f and f} + \Delta f \times \text{velocity}}{\text{Distance}} \right)$$

$$= \frac{\hbar\omega\Delta f}{e^{\frac{\hbar\omega}{kT}} - 1} \approx kT\Delta f \quad \text{for } \hbar\omega << kT \qquad (3.6)$$

If the power delivered to a matched load of resistance R by a mean-square voltage $\overline{v}_N^2$ is set equal to equation (3.6) the following result for the mean-square noise voltage for a resistor of value R is obtained:

$$\overline{v}_N^2 = 4kTR\Delta f \qquad (3.7)$$

This implies a model of a noisy resistor of the form:

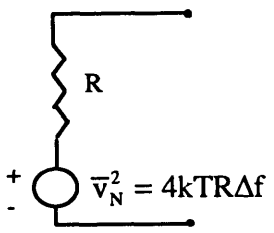

Figure 3.4: Noisy resistor model.

3.2 Intensity Correlation Spectrum

The starting point in the derivation of noise spectra is the set of equations known as the Quantum Langevin Equations [20]:

$$\dot{A}_s + (\gamma_s + \mu_s)A_s = 2\chi A_p A_i^+ + \sqrt{2\gamma_s}A_s^{in} + \sqrt{2\mu_s}B_s^{in} \qquad (3.8a)$$

$$\dot{A}_i + (\gamma_i + \mu_i)A_i = 2\chi A_p A_s^+ + \sqrt{2\gamma_i}A_i^{in} + \sqrt{2\mu_i}B_i^{in} \qquad (3.8b)$$

$$\dot{A}_p + (\gamma_p + \mu_p)A_p = -2\chi A_s A_i + \sqrt{2\gamma_p}A_p^{in} + \sqrt{2\mu_p}A_p^{in} \qquad (3.8c)$$

Here A_m is the slowly-varying time envelope for each of the internal field modes, γ_m the single pass loss parameter associated with the mirrors, μ_m the single pass loss parameters due to all other causes, χ the nonlinear coupling parameter, and A_m^{in} and B_m^{in} the incoming fields associated with the coupling mirrors and internal losses respectively. The second term on the left hand side of each equation may be viewed as a damping term, the first

and second terms on the right hand side as driving terms, and the last term on the right hand side as noise terms.

The γ_m are related to the amplitude reflection and transmission coefficients by:

$$r_m = 1 - \gamma_m \tag{3.9a}$$

$$t_m = \sqrt{2\gamma_m} \tag{3.9b}$$

Once the internal fields are solved for, the external fields may be derived using:

$$A_m^{out} = t_m A_m - A_m^{in} \tag{3.10}$$

The stationary field solutions are found by setting the derivatives and input terms for the signal and idler to zero, yielding:

$$\kappa_m \left|\overline{A}_m\right|^2 = \frac{\kappa_p \kappa_s \kappa_i}{4\chi^2}(\sigma - 1) \text{ for } \sigma \equiv 2\sqrt{\frac{2\chi^2 \gamma_p}{\kappa_p^2 \kappa_s \kappa_i}} A_p^{in} \tag{3.11}$$

$$\left|\overline{A}_m\right|^2 = \frac{\kappa_s \kappa_i}{4\chi^2} \tag{3.12}$$

where $\kappa_m \equiv \gamma_m + \mu_m$ and $\overline{A}_m$ is the mean (steady-state) field and m = s or i.

Note that the ratio of the output intensities of the signal and idler is given by:

$$\frac{\overline{I}_s^{out}}{\overline{I}_i^{out}} = \frac{\gamma_s \kappa_i}{\kappa_s \gamma_i} \tag{3.13}$$

In the absence of any internal loss ($\mu_{s,i} = 0$) this quantity is equal to one. This is reasonable since any photons created in the cavity must couple out regardless of any difference in the coupling constants. This equation also indicates the importance of keeping the losses well balanced.

Equations (3.8a-c) may now be linearized around the mean values of equations (3.11) and (3.12) by setting $A_m = \overline{A}_m + \delta a_m$ and $B_m = \overline{B}_m + \delta b_m$ resulting in:

$$\delta\dot{a}_s + \kappa_s \delta a_s = \sqrt{\kappa_s \kappa_i}\,\delta a_i^+ + \sqrt{\kappa_s \kappa_p(\sigma - 1)}\,\delta a_p + \sqrt{2\gamma_s}\,\delta a_s^{in} + \sqrt{2\mu_s}\,\delta b_s^{in} \qquad (3.14a)$$

$$\delta\dot{a}_i + \kappa_i \delta a_i = \sqrt{\kappa_s \kappa_i}\,\delta a_s^+ + \sqrt{\kappa_i \kappa_p(\sigma - 1)}\,\delta a_p + \sqrt{2\gamma_i}\,\delta a_i^{in} + \sqrt{2\mu_i}\,\delta b_i^{in} \qquad (3.14b)$$

$$\delta\dot{a}_p + \kappa_p \delta a_p = -\sqrt{\kappa_p \kappa_i(\sigma - 1)}\,\delta a_i^+ - \sqrt{\kappa_s \kappa_p(\sigma - 1)}\,\delta a_s + \sqrt{2\gamma_p}\,\delta a_p^{in} + \sqrt{2\mu_p}\,\delta b_p^{in} \qquad (3.14c)$$

We may now define a quantity (having chosen the mean fields to be real) $p_m = \delta a_m + \delta a_m^+$ which gives the field amplitude fluctuations. Further defining and solving for a quantity $r = \frac{1}{\sqrt{2}}(p_s - p_i)$, which for the balanced case of $\mu_s = \mu_i$ and $\gamma_s = \gamma_i$ yields:

$$\dot{r} + 2\kappa\, r = \sqrt{2\gamma}\, r^{in} + \sqrt{2\mu}\, r'^{in} \qquad (3.15)$$

where $r' = \frac{1}{\sqrt{2}}(p_s' - p_i')$ and $p_m' = \delta b_m + \delta b_m^+$.

The most salient point to note here is that (in the balanced case) this equation is independent of the pump field fluctuations. Fourier transforming equation (3.15), and

taking the magnitude square (with r^{in} and r'^{in} assumed to be independent random variables of normalized variance equal to one) yields:

$$S_I(\omega) = S_o \frac{4\mu\kappa + \omega^2}{4\kappa^2 + \omega^2} \tag{3.16}$$

where S_o is the shot noise of a beam with an intensity equal to the sum of the intensities of the signal and idler beams. Evaluation of this equation verifies some earlier qualitative points. There is significant noise suppression only over the cavity bandwidth ($\omega < 2\kappa$). When there is no loss, the shot noise is completely suppressed, at least at zero frequency. In the presence of cavity loss the minimum noise is $\frac{\mu}{\mu + \gamma}$; this is precisely the proportion of photons that are created that do not reach the photodetector (assuming perfect detection). From this ratio it is clear that losses due to causes other than output coupling must be kept small relative to the output coupling. In theory, large correlation can still be achieved for a lossy system by making the output coupling very large. Recall, however, from equation (2.18) that the oscillation threshold is proportional to the square of the losses. Making the output coupling too large can easily make the threshold condition unobtainable with any reasonable amount of pump power. Once again the overwhelming importance of keeping losses small is highlighted.

The assumption of perfectly balanced channels and doubly resonant fields gives instructive results, but is fairly unrealistic. For the most general case of unbalanced channels and detuned fields the method of solution [19] as outlined above remains the same, but is tedious, uninformative and yields unwieldy expressions. Rather, here it is best to qualitatively examine the effects of these non-idealities.

If the system is still balanced, but the cavity detuned, then it turns out that a non-trivial mean-field solution exists as long as the round trip phases of the signal and idler are equal (this manifests itself physically as mode clusters as will be shown on the following chapter). The resultant equation is precisely the same as equation (3.15). It is independent

once again of pump fluctuations as well as the round-trip phase deviation from resonance.

When the fields are on resonance, but unbalanced, there are two cases to consider. A shot noise limited pump yields a large increase (above shot noise) in low frequency noise with the maximum correlation occurring at about .1 to .2 times the cavity linewidth. Increasing the pump intensity to about 1.5 times threshold greatly diminishes this effect for typical loss values. In the presence of excess pump noise a large increase of low frequency noise (above shot noise) manifests itself, regardless of pump power. This effect is prominent only over those frequencies in which the pump noise is also significant.

In the case of unbalance and signal/idler detuning, the noise increase is minimal for small detunings, but increases sharply (especially, once again, for low frequencies relative to the cavity linewidth), as one might expect, for detunings nearing OPO cut-off. Even in the case of large detuning, however, some correlation is observable at frequencies above zero. Pump field detuning has minimal effect on the observed spectrum for pump powers of practical interest.

One final, perhaps paradoxical, result is worthy of mention. In the presence of unbalance in the two channels a partially reflecting mirror may be introduced in the path of the most intense beam to externally balance the beams. This has the adverse effect of coupling vacuum noise in through the unused port, but this effect is minimal when compared to the decrease witnessed in the transmitted pump noise. Hence, the introduction of external losses can actually improve the observed correlation for a practical experimental set-up.

CHAPTER 4

EXPERIMENTS

In this chapter the characterization of the OPO, the detection system, the experimental procedures used, and the quantum noise correlation results will be presented. The potassium titanyl phosphate (KTP) crystal is described in section 4.1. In section 4.2 the characterization of the crystals, and a variety of the mirrors that were considered for use, will be discussed. In section 4.3 the design of the detection circuitry, to include the summing and differencing circuits, will be explained. The point of the feedback stabilization of the two- and three-piece OPOs will be taken up in section 4.4. In section 4.5 the experimental set-up is explained leading do the presentation and discussion of results in section 4.6.

4.1 The KTP Crystal

Three crystals were used in the course of this work. Two were cut at $\theta = 90°$, $\phi = 23.18°$ and the other at $\theta = 90°$, $\phi = 28.13°$ where ϕ is measured from the crystallographic a-axis (material x- axis) and θ from the crystallographic c-axis (material z-axis). Of the two $\phi = 23.18°$ crystals one was hydrothermally grown (this crystal was used in the three-piece

OPO) and the other flux grown (this crystal was used in the two-piece OPO). The crystal cut ensures proper phase matching as explained in Chapter 2.

KTP is a preferred nonlinear material due to its strong nonlinear coefficients. Also, type-II phase matching for the frequencies of interest is easily obtained in KTP; the orthogonality of the signal and idler polarizations greatly simplifies the detection scheme as the two beams may be separated by a beam splitting polarizer. The d coefficients have the following values [21]:

$d_{31} = 2.54\text{pm/V}$

$d_{32} = 4.35\text{pm/V}$

$d_{33} = 16.9\text{pm/V}$

$d_{24} = 3.64\text{pm/V}$

$d_{15} = 1.91\text{pm/V}$

For type-II phase matching d_{eff} is given by:

$$d_{eff} = (d_{24} - d_{15})\sin 2\phi \sin 2\theta - (d_{15}\sin^2\phi + d_{24}\cos^2\phi)\sin\theta$$

The Sellmeir equations (empirical equations used to determine the indices of refraction for the three axes) are defined as (for KTP):

$$n_x^2 = 3.0065 + \frac{.03901}{\lambda^2 - .04251} - .01327\lambda^2$$

$$n_y^2 = 3.0333 + \frac{.04154}{\lambda^2 - .04547} - .01408\lambda^2$$

$$n_z^2 = 3.3134 + \frac{.05694}{\lambda^2 - .05658} - .01682\lambda^2$$

which give at the wavelengths of interest:

	n_x	n_y	n_z
$\lambda = 1.06\mu m$	**1.7377**	**1.7453**	**1.8297**
$\lambda = .531\mu m$	**1.7780**	**1.7886**	**1.8887**

The differences in the refractive indices result in a phenomena known as walk-off. When a beam walks-off the direction of propagation of the phase velocity (i.e. the direction of the k-vector) is not collinear with the direction of energy propagation. It has been shown by Boyd and Kleinman [14] that such walk-off for focused Gaussian beams reduces the conversion efficiency (as well as possibly, in our case, the intensity correlation). It is clear, however, that reduced conversion efficiency increases oscillation threshold, forcing a reduction in the percent output coupling for a given amount of available pump power, which as explained in Chapter 2, does reduce the amount of observable correlation. It was hoped that the crystal cut at $\theta = 90°$, $\phi = 28.13°$ would compensate for walk-off as has been observed in an internally doubled YAG laser that uses KTP as the second-harmonic generation crystal [16]. The difference in n_x and n_y is small, so that E-fields in the x-y plane are referred to as ordinary, and those with components along the z-axis are called extraordinary (conventionally, $n_z > n_y > n_x$).

4.2 Characterization

As described in previous chapters, cavity losses are of paramount concern. The best measure of overall cavity losses for a given optical parametric oscillator is the oscillation threshold power, or the amount of correlation it generates. It is, however, unwise to assemble the OPO without first getting some idea as to whether the various components of the cavity are at least within some reasonable tolerances. Further, the determination of threshold alone does not provide information as to the source of a problem; i.e. is the loss

due to absorption loss in the crystal, reflection at the crystal faces, or absorption/scattering/coupling losses at the mirrors?

The first order of business was to establish the quality of the anti-reflection coatings on the crystals. The following experimental set-up was used:

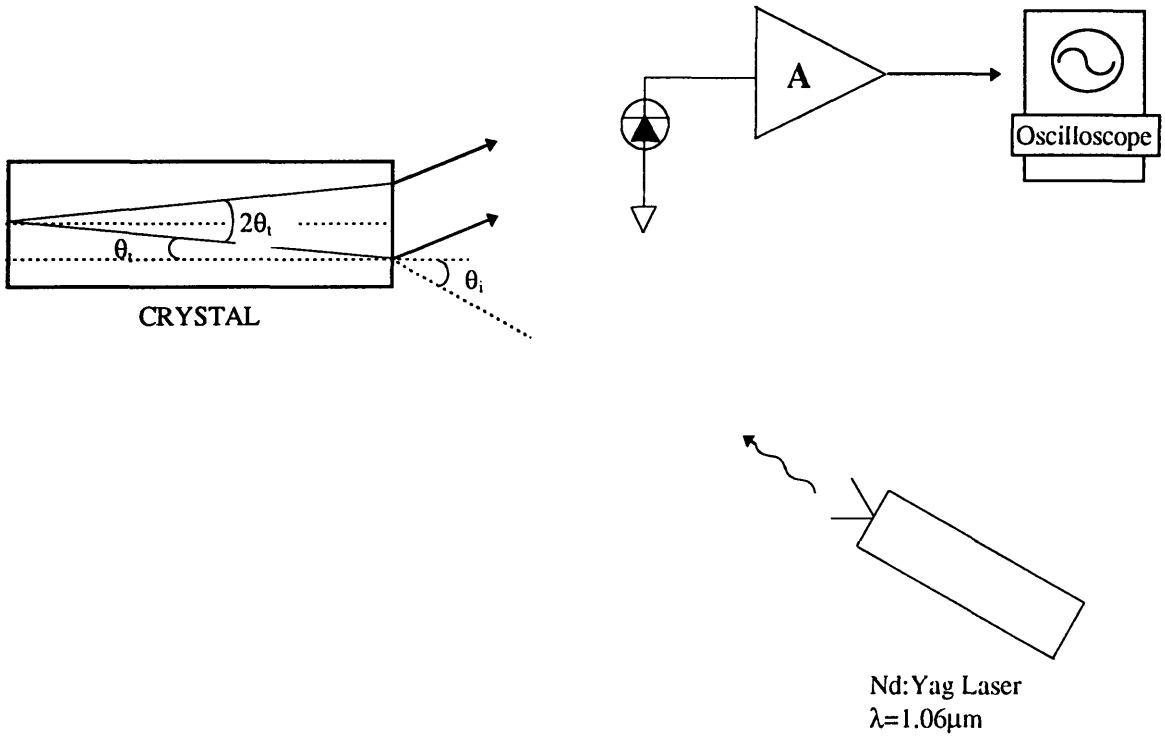

Figure 4.1: Measurement of crystal surface reflection coefficients.

In figure (4.1) the output of the laser was measured through a filter of known attenuation (the reflection coefficients of the crystal faces are quite small so laser power far in excess of what is necessary to saturate the photodiodes is required). This same beam was shown onto the crystal face, at a slight angle, and the reflected power measured. It is desirable to keep the angle of incidence small as large angles degrade the measurement accuracy.

Initial measurements resulted in values of reflectivity approximately twice that of manufacturers specifications. It was subsequently realized that the reflection from the rear crystal face was adding to the reflection from the front surface. Increasing the angle of incidence to approximately 12°~14° allowed for clear visual separation of the beam spots from the front and rear surfaces. Once this was accomplished, the measured reflection coefficients were much closer to quoted values. Since this is a rather large value of incident angle, it is likely that the reflection coefficients for normal incidence are actually smaller than those measured here.

Since the KTP crystal is biaxial, the refractive indices seen by the two orthogonal polarizations (along the ordinary and extraordinary axes) are different. As a result we measured the reflection for both polarizations, as well as for both crystal surfaces. The following results were obtained for the four potassium titanyl phosphate crystals coated by the companies shown with the crystal cut as given:

CRYSTAL ($\theta = 90^{o}$)	Reflectivity ∥ to Optic Axis	Reflectivity ⊥ to Optic Axis
Airtron-coated; hydrothermally grown $\phi = 23.18°$	**.031**	**.025**
Thin Film Labs-coated; flux grown $\phi = 23.18°$	**.080**	**.040**
Thin Film Labs-coated; flux grown $\phi = 28.13°$	**.081**	**.045**
Thin Film Labs-coated; flux grown $\phi = 0^{\circ}$	**.070**	**.120**

Table 4.1: Measured values of crystal surface reflection coefficients.

The Airtron hydrothermally grown crystal was designated for use in the 3-piece OPO, while the flux grown (obtained from Skytek) $\phi = 23.18°$ crystal was sent to have a mirror polished onto one end (by Airtron) for use in the 2-piece OPO. Airtron has provided the better product but at a significant cost differential.

A walk-off compensated scheme has previously been used in an internally doubled Nd:YAG laser that uses KTP as the second harmonic generation crystal [15], to minimize the effect of walk-off and to increase conversion efficiency. It was hoped that the same type configuration could be used in a down-conversion configuration to reduce the threshold in a 3-piece OPO. This crystal arrived damaged and was repolished and recoated. Since the losses at the crystal faces were much larger than those for the noncompensated Airtron crystal it was uncertain whether an improvement would be realized in practice, although any improvement could be determined theoretically by subtracting off other known losses. The crystal cut at $\theta = 90°$, $\phi = 0°$ was not intended for use in this experiment but rather served as a check on Thin Film Labs processing.

In order to determine mirror and crystal absorption losses the transmission properties of the Fabry-Perot cavity were utilized. If one considers an optical cavity of the form:

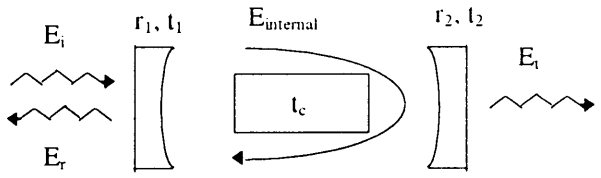

Figure 4.2: Fabry-Perot cavity.

where $r_{1,2}$, $t_{1,2}$ are the field reflection and transmission coefficients for the front and rear mirrors, respectively, t_c the field transmission coefficient for the crystal, E_i is the incident field, E_r the reflected field, E_t the transmitted field, and $E_{internal}$ the circulating internal

field. Looking at the ratio of the transmitted to incident field and assuming a phase shift ϕ for each pass it is found:

$$\frac{E_t}{E_i}(\phi) = t_1 t_c t_2 e^{j\phi} + t_1 t_c r_2 t_c (-r_1) t_c t_2 e^{j3\phi} + \cdots$$

$$= t_1 t_2 t_c e^{j\phi}\left(1 + (-r_1)(r_2)t_c^2 e^{j2\phi} + \left((-r_1)(r_2)t_c^2 e^{j2\phi}\right)^2 + \cdots\right)$$

$$= \frac{t_1 t_2 t_c e^{j\phi}}{1 + r_1 r_2 t_c^2 e^{j2\phi}} \qquad (4.1)$$

Taking the magnitude square of equation (4.1) and making the substitutions $|r_i|^2 = R_i$, and $|t_i|^2 = T_i$ along with appropriate trigonometric identities results in:

$$\left|\frac{E_t}{E_i}\right|^2(\phi) = \frac{T_1 T_2 T_c}{(1 - \sqrt{R_1 R_2 T_c})^2 + 4\sqrt{R_1 R_2 T_c}\sin^2\phi} \qquad (4.2)$$

Maximal transmission occurs when $\phi = m\pi$, where m is a non-zero positive integer. The spacings between transmission peaks, $\Delta\phi = \pi$, is known as the free spectral range (FSR) of the cavity . A useful measurement of the quality of the cavity is the full width at half-maximum (FWHM) as defined by FWHM $= 2\tilde{\phi}$ where $\left|\frac{E_t}{E_i}\right|^2(\tilde{\phi}) = \frac{1}{2}\left|\frac{E_t}{E_i}\right|^2_{max}$ and $\tilde{\phi}$ is given as:

$$\tilde{\phi} = \frac{1 - \sqrt{R_1 R_2 T_c}}{2\sqrt{\sqrt{R_1 R_2 T_c}}} \qquad (4.3)$$

where for a narrow resonance the approximation $\sin\phi \approx \phi$ is used.

The finesse F is defined as:

$$F \equiv \frac{FSR}{FWHM} = \frac{\pi}{2\tilde{\phi}} = \frac{\pi\sqrt{\sqrt{R_1 R_2}\,T_c}}{1-\sqrt{R_1 R_2}\,T_c} \qquad (4.4)$$

The experimental set-up for the finesse measurement is as follows:

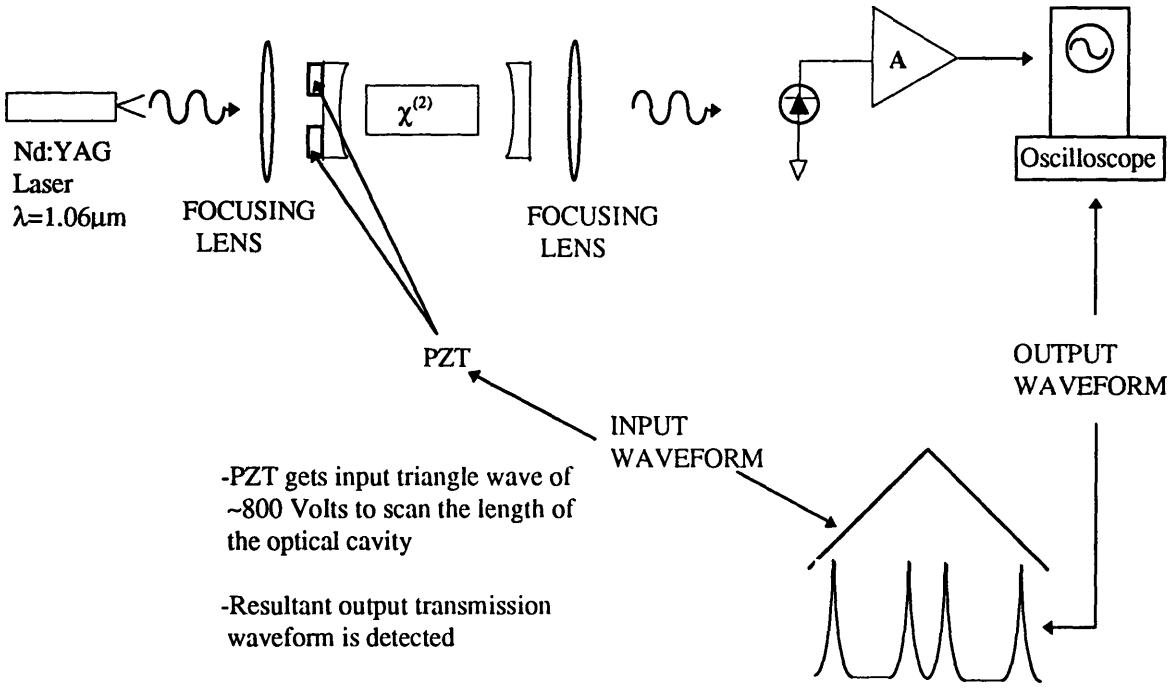

Figure 4.3: Experimental set-up for cavity finesse measurement.

The cavity is aligned by first passing the source beam through the center of the crystal at normal incidence (if a crystal is being used in the measurement). Then the back mirror is aligned so that the reflected beam exactly coincides with the incident beam. The plates holding the mirrors that attach to the body of the cavity have oversized holes drilled in them to allow such freedom of movement. The front mirror is then positioned and aligned by looking for transmission through the cavity. Since all sources are in the infrared it is necessary to use an IR scope to make these alignments.

In this set-up, the optical cavity length is scanned by applying a triangle wave with an amplitude of several hundred volts across piezo-electric transducers (PZT). The PZT's expand at a rate of approximately 500 picometers/volt. The length change must be enough to scan through at least one FSR. The frequency of the scanning input is approximately 30 Hz. Faster scan rates skew the output waveform indicating the PZT cannot move the mass of the mirror quickly enough. The detected output waveform is recorded on a LeCroy 9400 digital oscilloscope. The FSR range is measured using the cursor function of the scope. By expanding the trace of the output, the FWHM can also be measured. In practice, due primarily to the nonlinearity of the PZT, the FWHM of each of the two peaks in the FSR are not equal. An average of the two is taken for each measurement. Also, due to various mechanical noise sources, the values of the FSR and average FWHM can vary from measurement to measurement for the same cavity; changes of as much as ± 40 for finesse values in the range of 500-650 are seen. Here again, several measurements are taken (typically 5 or 6 for each set-up) with the average value taken as the finesse for a given cavity. Examples of the output waveforms are given in figure (4.4).

In the case of high finesse cavities (F > several hundred) it was necessary to scan over the resonance peaks more slowly. The FSR was determined as described in the latter paragraph, then the scan rate and range were adjusted so as to scan slowly over one of the two transmission maxima in the FSR. In this way, artificial broadening of the peak due to PZT inertia and/or nonlinearity was minimized.

From the finesse measurement the losses may be approximated by starting with equation (4.4) and taking $R_2 = 1$ and $R_1 = R$. This is tantamount to lumping the losses of both mirrors into one of the mirrors. This is justified for $R_1, R_2 \approx 1$. This yields:

$$F = \frac{\pi\sqrt{\sqrt{R_1 R_2}T_c}}{1-\sqrt{R_1 R_2}T_c} \cong \frac{\pi\sqrt{\sqrt{R}T_c}}{1-\sqrt{R}T_c} \qquad (4.5)$$

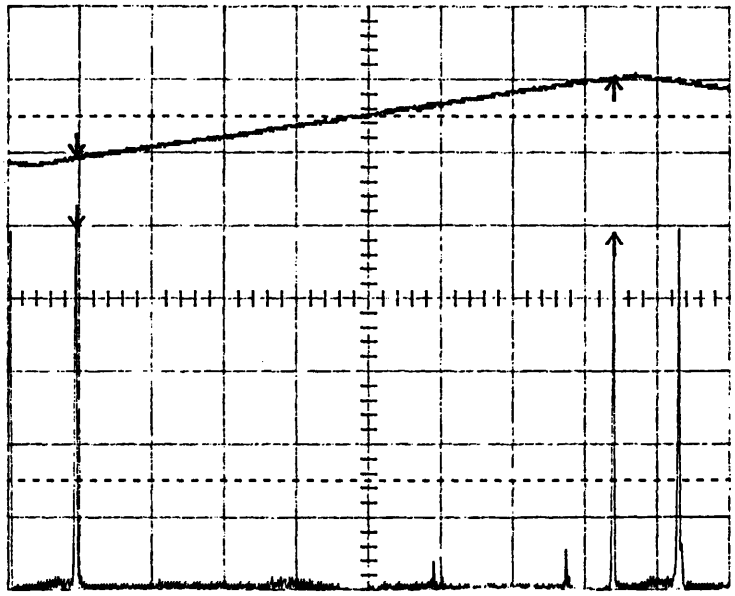

Figure 4.4a

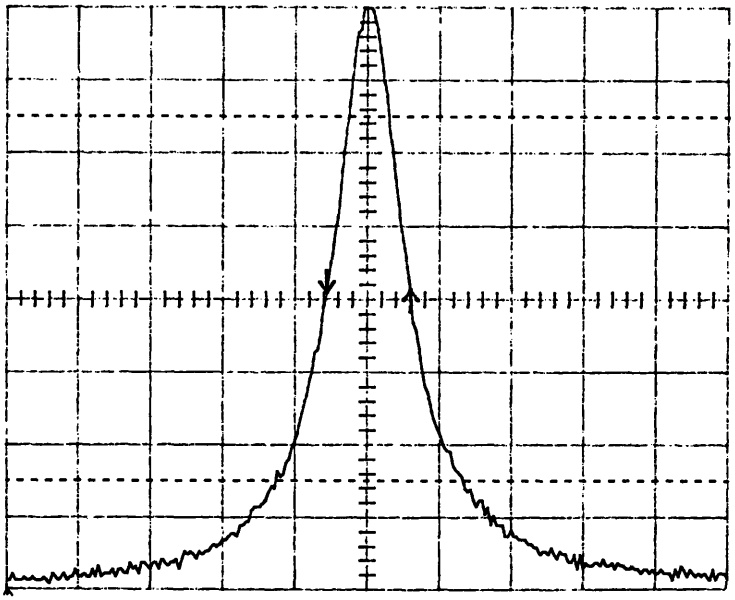

Figure 4.4b

Figure 4.4: a) A typical finesse measurement. The top trace is the triangular waveform driving the PZT (5 V/div). The bottom waveform represents the output from the OPO (10mV/div). The timescale is 2ms/div. b) An expansion of one of the transmission peaks.

The numerator is very close to being equal to π for typical values of R and T_c. For the mirror we can write:

$$R + T + L = 1 \tag{4.6}$$

where L is the mirror loss. Similarly for the crystal:

$$R_c + T_c + L_c = 1 \tag{4.7}$$

Making these substitutions and keeping terms only to first order gives:

$$F \approx \frac{\pi}{1-\sqrt{1-(T+L)}(1-L_c)} \approx \frac{\pi}{1-\left(1-\frac{T+L}{2}\right)(1-L_c)}$$

$$\approx \frac{\pi}{1-\left(1-L_c-\frac{T+L}{2}+\Theta(2)\right)} \approx \frac{2\pi}{T+L+2L_c} \tag{4.8}$$

Hence, by measuring the finesse for various cavity configurations as well as the transmission coefficients of the mirrors, the losses of the mirrors and crystals may be found. Further, by subtracting off the measured reflection coefficients of the crystal faces, the absorption losses in the crystals may be found.

As mentioned previously, the PZT's are nonlinear and the value of the full width at half maximum is determined as the average of two values. In order to ensure that the values that were obtained for the losses of the mirrors and crystals were reasonably accurate a method was devised that removed the nonlinearity of the PZT from the measurement. To do this the reflected, rather than the transmitted, intensity was observed. Using an analysis similar as that used to find equation (4.1), but for the reflected field, and

employing the approximations used enroute to equation (4.8) it is found that the ratio of the reflected field E_r to the incident field E_i is:

$$\frac{E_r}{E_i} \cong \frac{1-\frac{1}{2}(T+L)+(1-(L+L_c))e^{j\phi}}{1+(1-\frac{1}{2}(T+L))e^{j\phi}} \tag{4.9}$$

Maximum reflection occurs at $\phi = \frac{\pi}{2}$ yielding:

$$\left|\frac{E_r}{E_i}\right|_{max} \cong \left|\frac{1-\frac{1}{2}(T+L)+j(1-(L+L_c))}{1+j\left(1-\frac{1}{2}(T+L)\right)}\right| \cong 1 \tag{4.10}$$

for L<<1.

The reflection minimum occurs at $\varphi = \pi$ and is given by:

$$\left|\frac{E_r}{E_i}\right|_{min} \cong \frac{L+2L_c-T}{L+2L_c+T} \tag{4.11}$$

If the ratio of the minimum to maximum reflected power is designated as P then:

$$P \cong \left(\frac{L+2L_c-T}{L+2L_c+T}\right)^2 \tag{4.12}$$

Defining the total loss as $L_T = L+2L_c$ and solving for this quantity gives:

$$L_T = \left(\frac{1 \mp \sqrt{P}}{1 \pm \sqrt{P}}\right) T \qquad (4.13)$$

From this equation one solution will either be inordinately high or low, implying only one correct solution. This result is purely a function of the minimum to maximum reflection ratios and hence independent of PZT nonlinearity. The experimental set-up for the reflection measurement looks as follows:

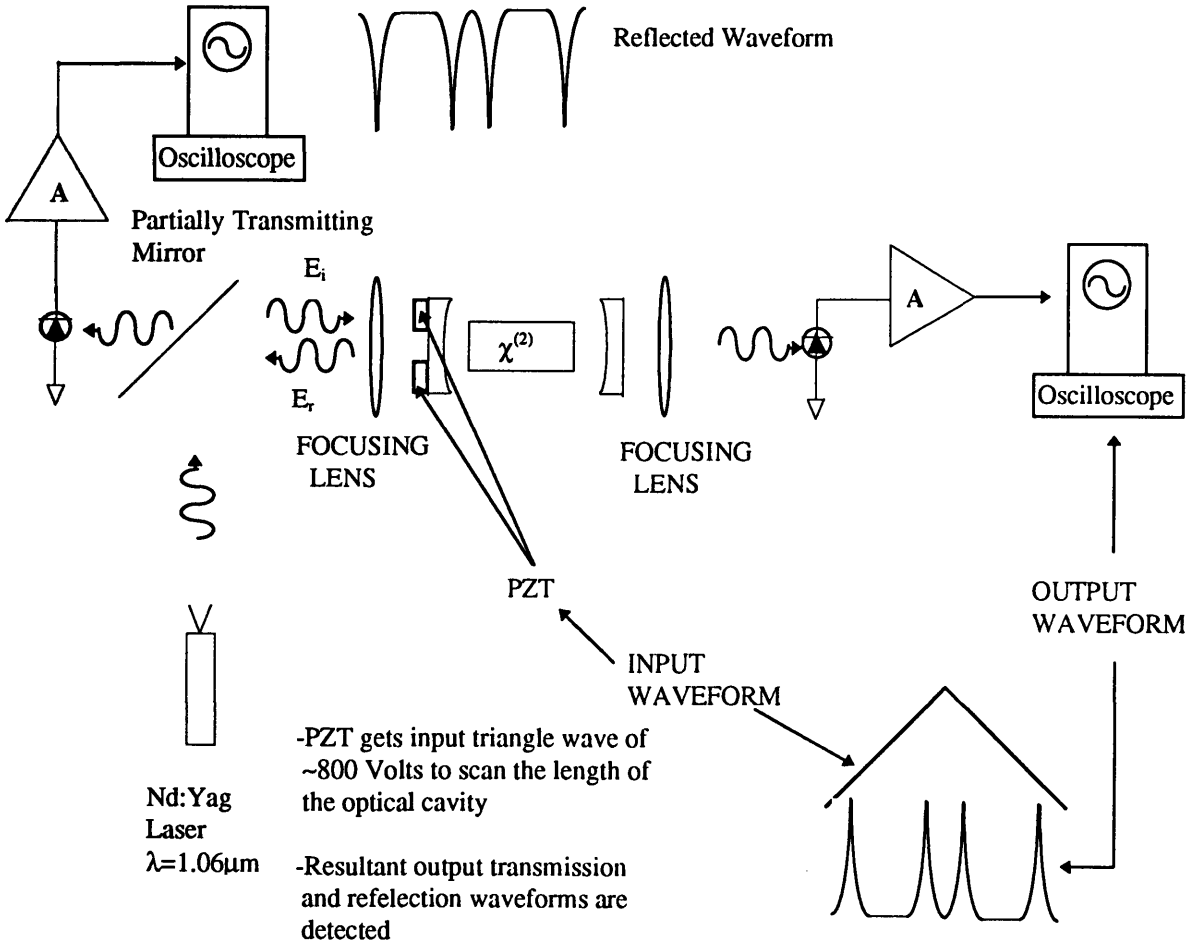

Figure 4.5: Reflection dip measurement experimental set-up.

The transmitted waveform was simultaneously monitored so that a finesse measurement taken from the transmission could be compared to that taken from the reflection. There was excellent agreement between the two in all cases. Initially, there were sharp differences in the losses that could be inferred from the finesse verses reflection measurements; well in excess of that which could be attributed to PZT's nonlinearity. A higher gain, less noisy photodiode/transimpedance amplifier was substituted for the photodiode/transimpedance amplifier detecting the reflected signal. As a result it was found that a small portion of the laser power was in modes other than the TEM_{00} mode as manifested by small reflection minima in regions between the fundamental minima (see figure(4.6)). When the measurements were corrected for this additional reflection very good agreement was found between the losses predicted by the finesse measurements and that from the reflection measurements. The reflection measurements were very difficult to align and hence are not the preferred loss measurement technique. Further, the finesse measurements were less sensitive to minor misalignments and the power in the higher order modes. However, the reflection measurements enable us to obtain the ratio of the internal losses to the output coupling.

It is important to note, for the measurements of cavities loaded with crystals, great care must be taken to avoid a multi-cavity effect between the mirrors and the crystal faces. In early measurements this effect resulted in measurements implying unrealistically low losses. To minimize the multi-cavity influence on measurement accuracy the crystals were mounted on rotary stages in the cavities so they could be rotationally perturbed.

Four different mirrors were tested. For the mirrors purchased from Airtron and Research Electro-Optics (REO), each of the three mirrors (a total of six mirrors) were individually measured to ensure uniformity within the lot. In each case, losses of the mirrors from the same manufacturer were very similar. With the exception of one mirror, all the mirrors tested had transmission coefficients for the Kr^{+}-ion pump laser (λ=.531 μm; visible green) in excess of 90%, and were very high reflectors for the infrared (λ=1.06 μm) with $R \approx 1$. In the three-piece cavity OPO the output coupler was designed for T=2.7% at

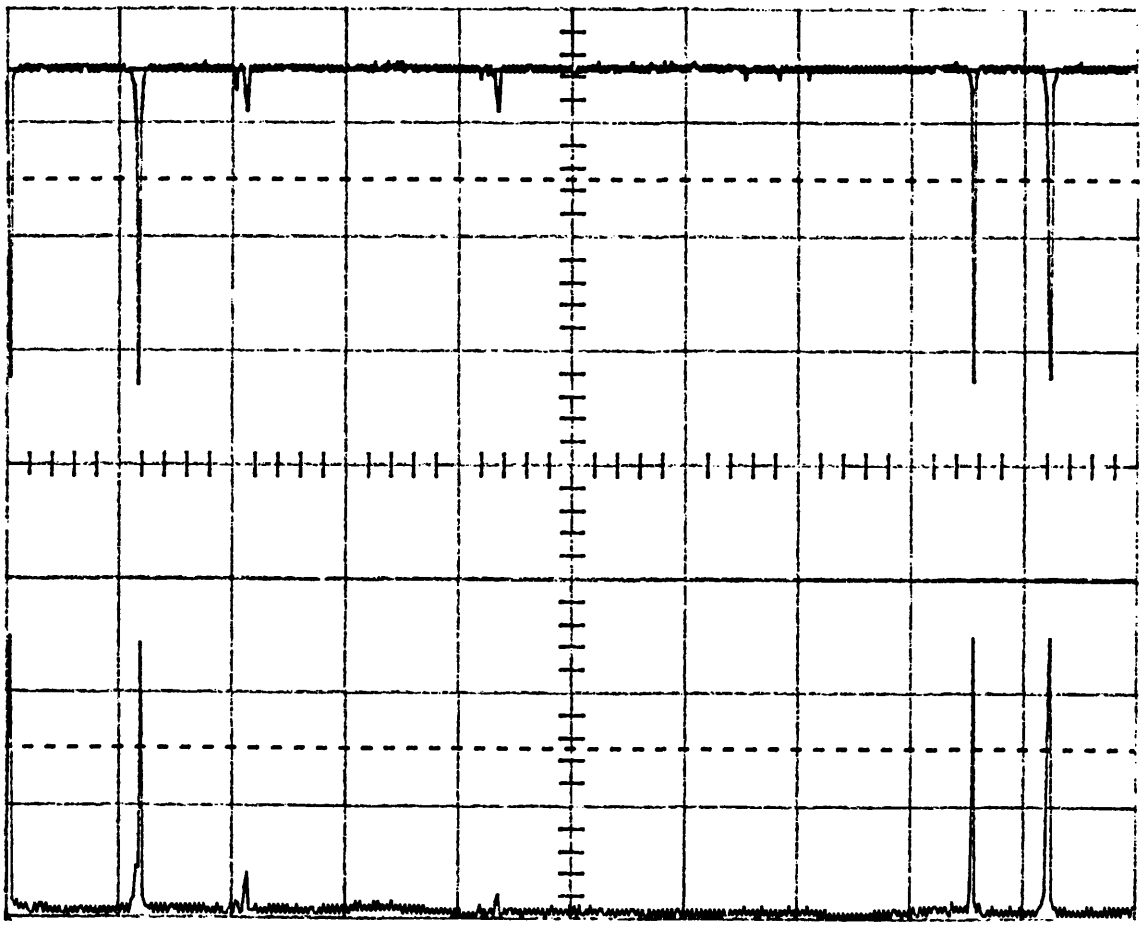

Figure 4.6: The upper trace is the reflected intensity (.2V/div). The zero for the reflected intensity is the third grid from the bottom. Note the small resonances between the major transmission maxima. The lower trace is the transmitted field (20mV/div). The timescale is 2ms/div.

λ=1.06 μm implying that any other losses due to mirror scattering or absorption would be inconsequentially small.

The fourth mirror was a high reflector for the green pump, and had a measured IR output coupling coefficient of .75%. This mirror was used in the early OPO configurations as the 2.7% output coupler had not yet arrived. Additionally, such a low output coupling does not dominate over other losses thus allowing the measured threshold of the OPO to be a further check of the total losses. With a transmission coefficient of only .75% it was, of course, necessary to determine the additional loss due to absorption/scattering in this mirror.

The cavities were set-up in a variety of mirror configurations, in all over twenty-five cavities were aligned and measured, until consistent results could be established. Cavities made of two high IR reflectivity mirrors proved very difficult to align, with finesses in excess of 5000. A cavity made of only REO mirrors could not be successfully aligned. Once the mirrors were well characterized, the crystal losses were also determined. A least squares fit was done for the measured data.

MIRROR	Radius of Curvature	Transmission Properties	LOSS @ λ=1.06 μm
Virgo Optics	**25mm**	**T=.75@λ=1.06 μm HR@λ=.532 μm**	**.11%**
Thin Film Lab	**20mm**	**HR@λ=1.06 μm T≈1@λ=.532 μm**	**.10%**
Airtron	**25mm**	**HR@λ=1.06 μm T=.96@λ=.532 μm**	**.05%**
Research Electro-Optics	**200mm**	**HR@λ=1.06 μm T=.98@λ=.532 μm**	**< .003% (estimated)**

Table 4.2: Measured mirror losses.

And for the crystal absorption losses:

CRYSTAL	Length and Cut	E ∥ $\hat{z}$	E ⊥ $\hat{z}$
Airtron	**10 mm ϕ = 23.18°**	**.05%**	**.04%**
Skytek/Thin Film	**12mm ϕ = 28.13°**	**.20%**	**.15%**
Skytek/Thin Film**	**12mm ϕ = 23.18° (Mirror of R=40mm polished on one end)**	**.03%**	**.04%**

Table 4.3: Measured crystal absorption losses.

** This crystal was measured in a cavity that was aligned as a lasing OPO and it was not possible to change the cavity to ensure a multi-cavity effect did not exist. The cavity finesse for both senses of polarization came out to be 650. The values of absorption loss are not unrealistic, but suspect.

4.3 The Detection Circuitry

The two components of primary consideration in the detection process were the photodiode and the operational amplifier to be used in the transimpedance amplifier. The photodiode chosen was an Epitaxx1000T InGaAs PIN photodiode. It possesses the following properties:

-η (quantum efficiency in electron-hole pairs/photon) of > 90%.
-Power dissipation of 100mW.
-Good linearity.
-A bandwidth of 70MHz for a 50Ω load.

The active diameter of the diode is 1mm. Such a large active area allows high optical power absorption with little concern for local saturation (the incident beam may be defocused). This large active area also has a sizable junction capacitance associated with it. Typically this is 100pF with no reverse bias, to roughly 30pF with a reverse bias in excess of 15 volts. The diodes purchased from Epitaxx were chosen from a production lot so as to have the largest quantum efficiency available. These diodes have unbiased capacitance's of 120-130pF. The capacitance of the diodes, as will be explained later, would prove to limit the detection bandwidth of our circuit.

The operational amplifier selected was the Comlinear CLC425. It is a BJT technology amplifier (rendering it considerably less costly than hybrid MOSFET-BJT amplifiers) with the following published specifications:

-Gain-Bandwidth Product (GBWP) of 1.7 GHz.
-1.05nV/$\sqrt{\text{Hz}}$ noise voltage density referred to the input.
-2.0pA/$\sqrt{\text{Hz}}$ noise current density referred to the input.

It was necessary to keep the noise of the detection circuitry as low as possible to get the best dynamic range. The largest apparent problem with the CLC425 rested with the small supply rails (± 5 Volts). This would normally render the highest allowable photocurrent to be ~4mA. To circumvent this problem, an input DC bias was used to offset the voltage generated by the photocurrent. This raised the maximum allowable signal to 6-8mA. If the biasing resistor is chosen to be large with respect to the feedback resistance, the additional noise contribution is small.

Two problems greatly exacerbated the development of the transimpedance amplifiers. One was the lack of a reliable SPICE model (since corrected by Comlinear) and the other the need to solder all components directly to the evaluation board as chip/component carriers introduced enough stray capacitance to have a sizable adverse effect on the frequency response of the amplifier for frequencies in excess of 20MHz. To address the latter, evaluation boards were purchased from Comlinear and suitably modified for this application.

A simplified model of the operational amplifier with noise sources was developed:

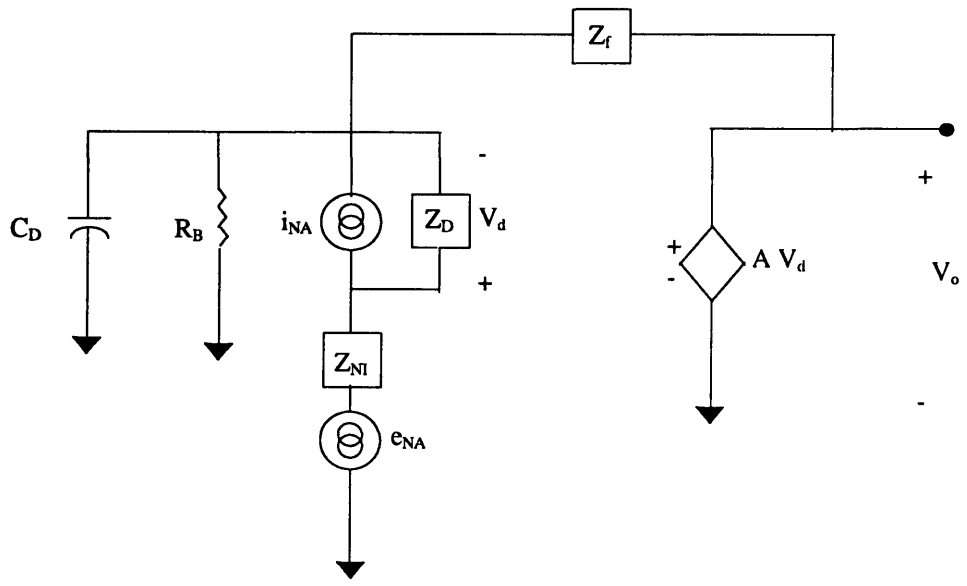

Figure 4.7: Model of transimpedance amplifier used to determine electronic noise spectrum.

where:

$$Z_i = \frac{R_i}{sR_iC_i + 1}$$

C_D = Capacitance of the photodiode.

R_B = The DC-offset biasing resistor.

e_{NA} = Voltage noise density of the op-amp.

i_{NA} = Current noise density of the op-amp.

A = Frequency dependent gain of the op-amp.

The series resistance and the junction resistance (which is very small compared to the biasing resistor) of the photodiode have been ignored as has the output resistance of the op-amp. Each noise source is statistically independent of the others. The transfer function for each noise source is then given as (assuming a voltage noise density of $\sqrt{4kTR}$ for each resistor (with the exception of the differential input resistance) as derived in Chapter 3):

For the non-inverting terminal resistance:

$$V_o = \frac{Z_d Z_{NI} \sqrt{4kTR_{NI}}}{\left(\frac{R_{NI}(Z_{NI} + Z_d)}{A} + \frac{(Z_d + \frac{Z_f}{A})R_{NI}}{(sC_D Z_f + 1)} \right)} \qquad (4.14)$$

For the biasing resistor:

$$V_o = -\frac{Z_f\sqrt{4kTR_f}}{\left(\frac{(Z_d + Z_{NI})(Z_f + sC_DR_BZ_f + R_B}{AZ_d} + R_B\right)} \tag{4.15}$$

For the feedback resistor:

$$V_o = -\frac{\sqrt{4kTR_f}}{\left(1 + \frac{(Z_d + Z_{NI})(Z_f + Z_d + Z_{NI})sC_D}{AZ_d}\right)} \tag{4.16}$$

For the amplifier noise voltage:

$$V_o = \frac{(sC_D(Z_{NI} + Z_d)Z_f + Z_f + Z_{NI} + Z_d)e_{NA}}{\left(Z_{NI} + Z_d + \left(\frac{Z_d + Z_{NI}}{AZ_D}\right)(sC_D(Z_{NI} + Z_d)Z_f + Z_f + Z_{NI} + Z_d)\right)} \tag{4.17}$$

For the amplifier noise current:

$$V_o = -\frac{(Z_{NI}(sC_DZ_dZ_f + Z_d) + Z_dZ_f)i_{NA}}{\left(\frac{Z_f}{A} + Z_d + \frac{(Z_{NI} + Z_d)(sC_DZ_dZ_f + Z_d)}{AZ_d}\right)} \tag{4.18}$$

In order to determine the total output noise each term is magnitude squared, divided by the 50Ω output resistance, and multiplied by a given resolution bandwidth. By letting $A \rightarrow \infty$ it is easy to see that at low frequencies the dominant source of noise is the feedback resistor, while at higher frequencies the diode capacitance C_D provides a dominant frequency dependent gain term for the amplifier voltage noise. It is this gain term that is responsible for the rapid noise floor rise at frequencies in excess of 5MHz limiting the useful bandwidth of the detection circuitry. Figure (4.7) shows the computed noise frequency response for :

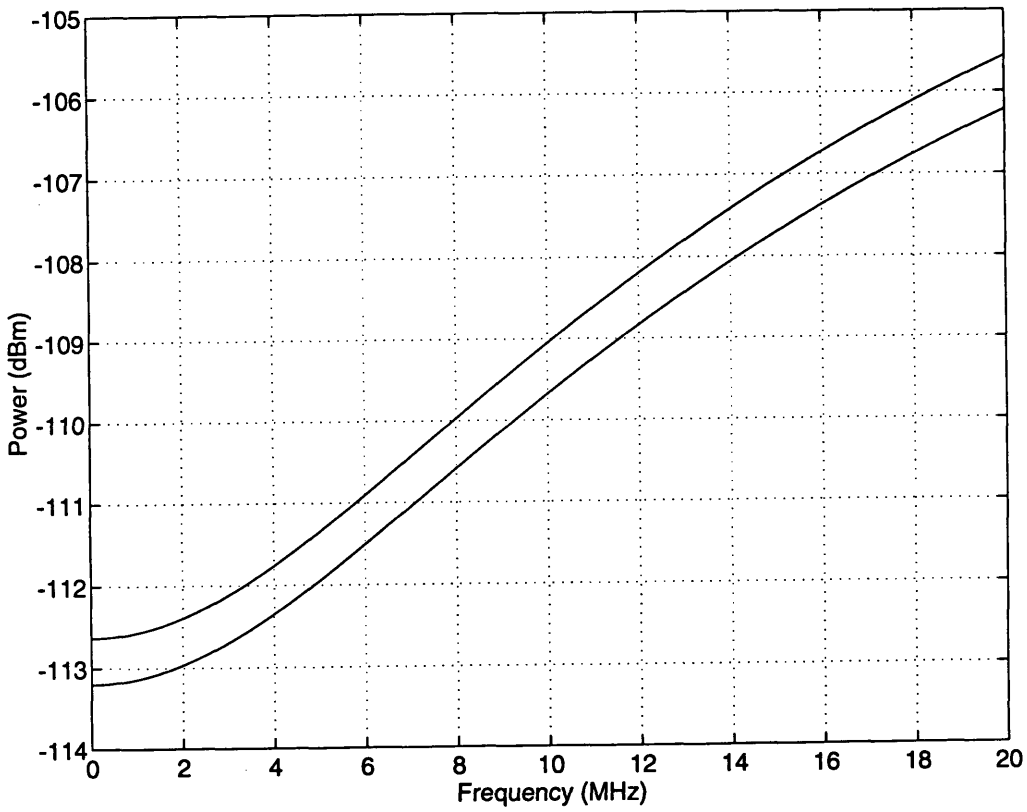

Figure 4.8: Computed noise floor for the circuit of figure 4.7 at 10 kHz resolution bandwidth. The upper trace is for the maximum specified values of e_{NA} and i_{NA}, while the lower trace is for the typical values of those quantities.

$R_{NI} = 100\Omega$

$R_B = 2.2k\Omega$

$R_f = 1k\Omega$

$R_d = 6k\Omega$ (R_d is the differential input resistance to the op-amp)

$C_D = 50pF$

$C_{NI} = 0$

$C_f = 5pF$

$C_d = 15pF$ (C_d is the differential input capacitance to the op-amp)

$e_{NA} = 1.05\ nV/\sqrt{Hz}$

$i_{NA} = 2pA/\sqrt{Hz}$

$$A \cong \frac{10^5 e^{-j\arg\left(\frac{s}{2\pi 10^6}+1\right)}}{\frac{s}{2\pi 10^5}+1} \frac{Volts}{Volt}$$

The upper trace gives the noise output of the maximum guaranteed limits for the CLC425 of $e_{NA} = 1.25\ nV/\sqrt{Hz}$ and $i_{NA} = 2.5pA/\sqrt{Hz}$. Figure (4.9a) shows the actual frequency response of the system. The difference in the two responses results from the differences in the capacitances of the photodiodes. The capacitances of the photodiodes were estimated by replacing the diode in the actual circuit with varying capacitor sizes until the responses of the two circuits nearly matched. Figure (4.9b) demonstrates the linearity of the system.

An interesting phenomena manifested itself during the transimpedance amplifier development prior to the derivation of this model. Comlinear suggests a minimum resistance at the non-inverting terminal of 25Ω. Through successive iteration the optimum value was empirically determined to be approximately 100Ω. Since it was known that sources at the non-inverting terminal see a frequency dependent gain it is clearly desirable to minimize any extra noise contribution at this terminal. Placing a by-pass capacitor across the non-inverting resistance seemed to be a reasonable solution to

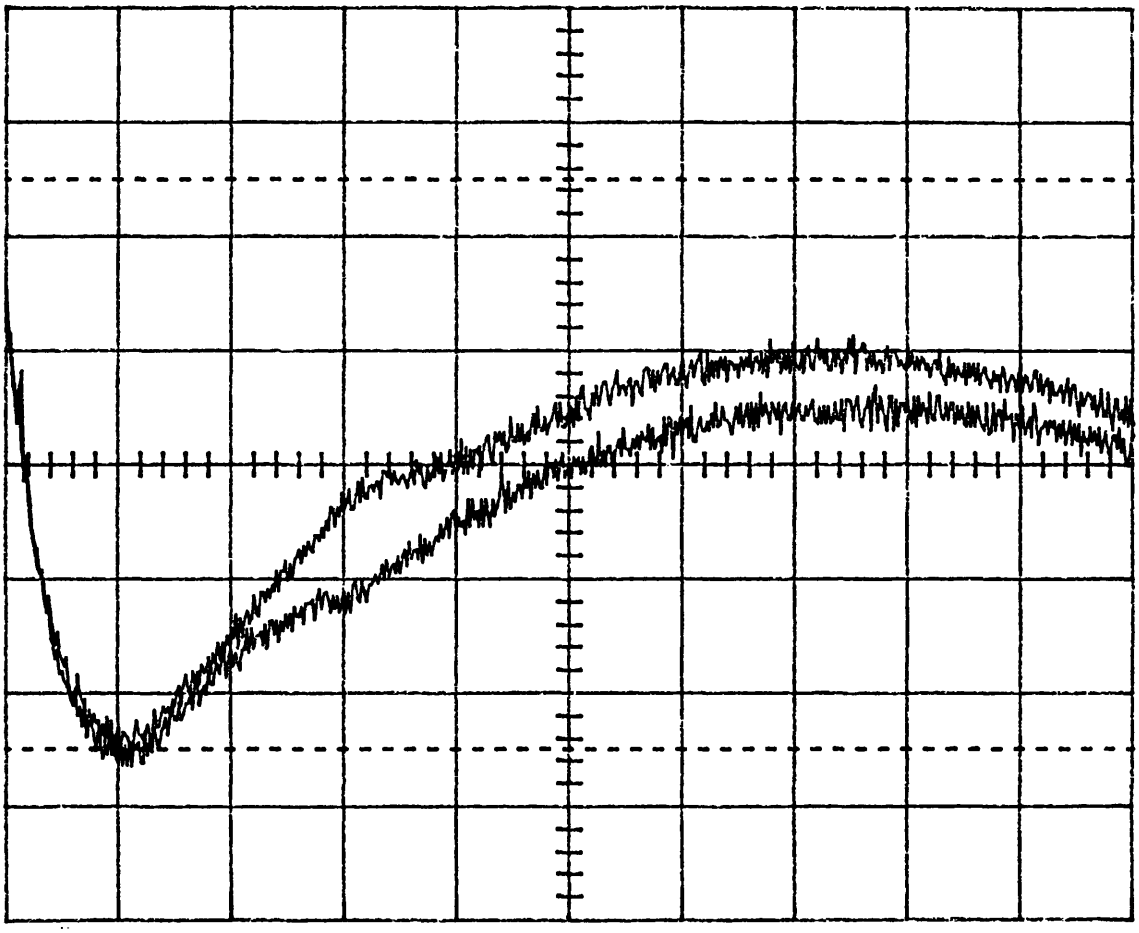

Figure 4.9: a) The frequency responses of the two transimpedance amplifiers. The differences in the traces result from the differences in the capacitance of the two photodiodes. The large low frequency noise is the 1/f noise of the spectrum analyzer. 5MHz/div; 0-50 MHz; 2dBm/div; 100kHz resolution bandwidth (RBW); the top grid line represents -92dBm.

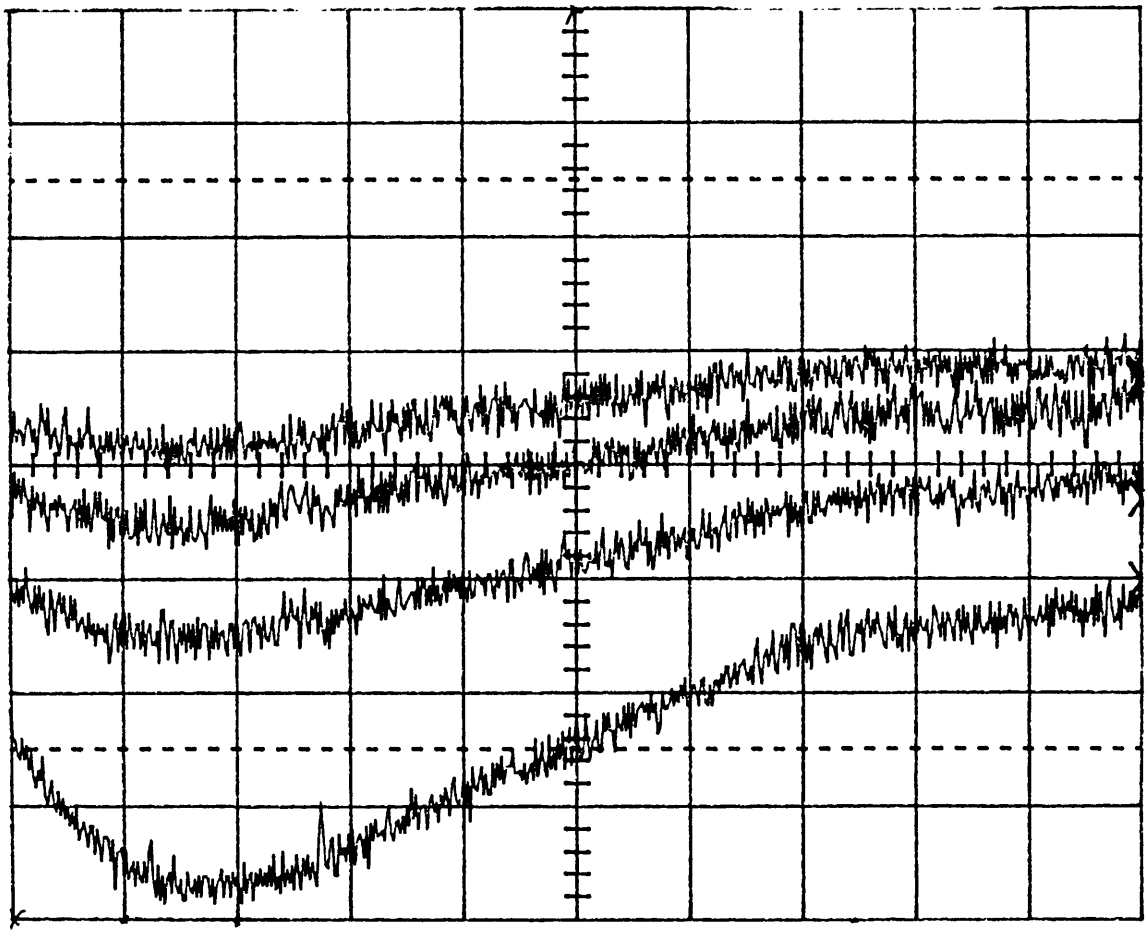

Figure 4.9:b) The linearity of the photodiode/amplifier is demonstrated for 1 through 3mA (top three traces) of white light generated photocurrent. The bottom trace is the noise floor of the spectrum analyzer plus transimpedance amplifier. 2MHz/div; 4-24MHz; 2dB/div; 100kHz RBW; the top grid is -89dBm.

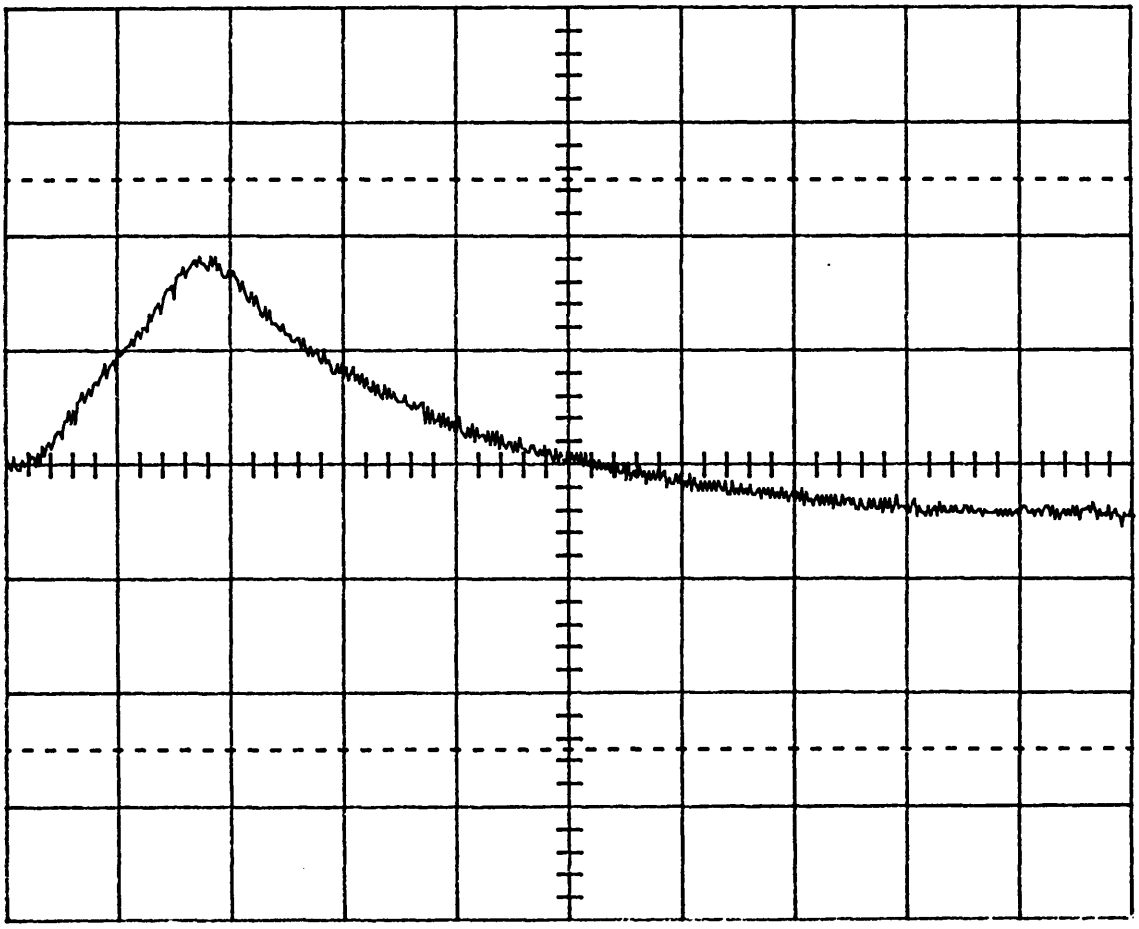

Figure 4.10: Frequency response of a transimpedance amplifier with a 2nF capacitor in parallel with 100Ω at the non-inverting terminal. 10MHz/div; 0-100 MHz; 10dB/div; 100kHz resolution bandwidth; the top grid line represents -62dBm.

this problem; DC stability would be ensured but the high-frequency noise contribution from the thermal noise would, in principle, be eliminated.

The actual response, however, was quite different than expected (figure(4.10)). The initial assumption was that an RLC-type resonance was being manifested. To test this hypothesis a wide range of non-inverting capacitance values were tried, each producing the same noise response, indicating that this result was not, in fact, due to a resonance. When a short was placed at the non-inverting terminal a similar response was measured. Apparently the lack of a high frequency resistance coupled the diode capacitance to the operational amplifier differential capacitance resulting in a significantly increased frequency dependent gain term. The excess noise introduced by this resistor must, therefore, be accepted. The model previously presented captures this phenomena out to about 20 MHz but not the roll-off beyond that point. This model was also not a good predictor of the cut-off frequency of the transimpedance amplifier. Both these shortcomings may be due to the single pole approximation of the CLC425 open loop gain transfer function.

The original design for the transimpedance amplifier was as shown in figure (4.11).

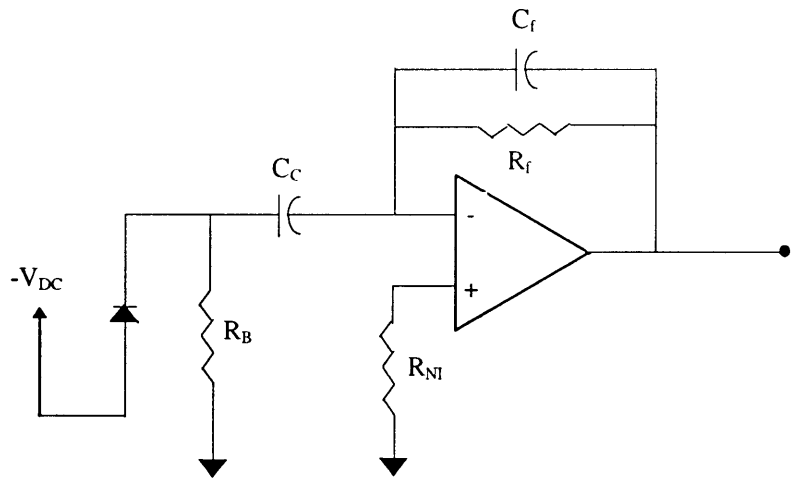

Figure 4.11: Initial design for transimpedance amplifier.

The advantage of this configuration is no DC current flows in the feedback path. In this way the disadvantage of the small ±5 Volt supply rails is overcome, while all AC portions of the signal (i.e. the shot noise) are coupled to the output through the coupling capacitor C_C. The initial photodiode DC bias was chosen to be 5Volts. With the photodiode possessing a power dissipation of 100mW this set-up would allow, in theory, 20mA of DC photocurrent to flow (in reality, saturation of the photodiode active area would most likely occur prior to this). The problem lies in the gain of $-\frac{R_f}{R_B}$ seen by the thermal voltage produced in R_B. If R_B is kept small, let's say 100Ω, so as to not upset the DC bias point of the photodiode when current flows in the system, then for a typical value of R_f = 1kΩ, the power gain (as the spectrum analyzer measures power) seen by the biasing resistor thermal source is 100. This significantly increases the noise floor and, consequently, markedly reduces the dynamic range.

In order to keep the effect introduced by R_B minimal it needs to be roughly twice the value of R_f. Assuming again R_f = 1kΩ, implying R_B = 2kΩ, the DC bias of the photodiode is forced to be increased to allow for any reasonable amount of photocurrent. The maximum allowable reverse voltage for the Epitaxx1000T is 20Volts. A safe voltage can then be taken as 15Volts which still allows over 6mA to flow while maintaining power dissipation less than 100mW. At 6mA photocurrent the reverse bias across the photodiode is decreased to 3Volts increasing the diode junction capacitance from a nominal 30pF to nearly 100pF. At best this sharply affects the frequency response of the noise floor, and at worst sends the amplifier into oscillations (the CLC425 is not internally compensated). The feedback capacitor (necessary for the stability of the amplifier) can be increased to allow for stability over all operating conditions but this would reduce the bandwidth of the system to less than 20 MHz, and would not alleviate the rapidly rising noise floor. Each of these observations was verified experimentally.

As such, the following system was adopted:

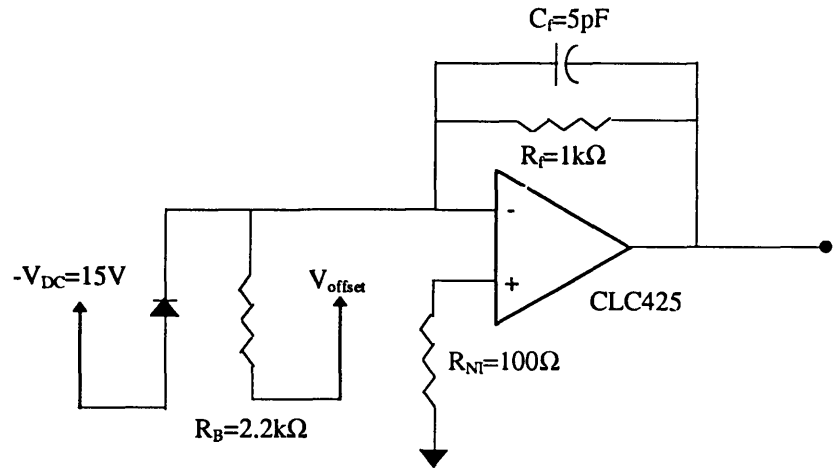

Figure 4.12: Final design of transimpedance amplifier.

In order to get 6mA of photocurrent it is only necessary to introduce an offset of -3 Volts at the output (~6 Volts at the input). For significantly larger values, the offset must be incremented up so as to never saturate the CLC425. This only adds a small additional experimental nuisance. The system is marginally stable at C_f = 2.7pF and is operated at C_f = 5pF to ensure absolute stability but a lesser value of ~3.5pF would work well. As shown, the bandwidth of the transimpedance amplifier is 40MHz.

In order to match the frequency characteristics of the CLC425's used in the transimpedance configuration a CLC425 was also used to perform the differencing operation. It proved nearly impossible to get broadband (in excess of 10MHz) phase differentials of 180° by using a differential amplifier configuration (i.e. one input into the inverting terminal and the other into the non-inverting terminal). For this reason the photodiode in the other detector is inverted with the polarity of V_{offset} and V_{DC} also switched. In this manner the voltages of the two channels can be subtracted by summing the outputs of the two transimpedance amplifiers. This method was experimentally shown to be the most efficacious.

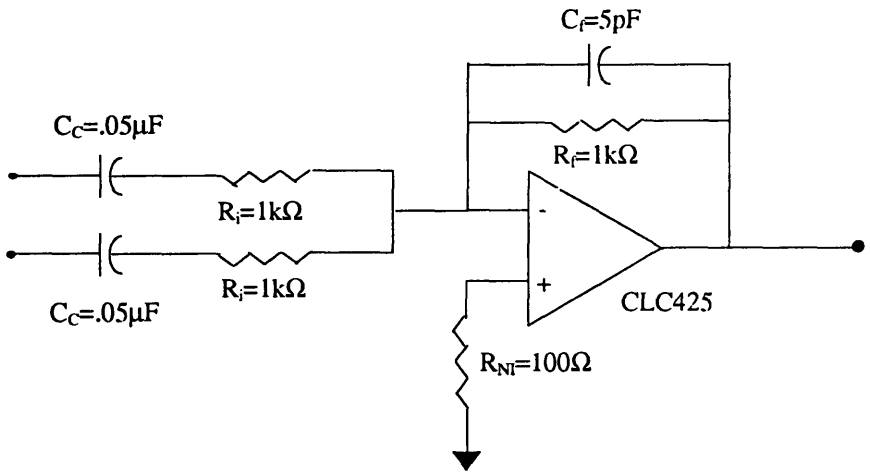

Figure 4.13: The summing amplifier.

The CLC425's that were used in the final transimpedance amplifiers had measured noise floors approximately 2dBm above that measured in the prototype device. The difference can only be attributed to amplifiers that fall outside of manufacturer specifications for noise. Comlinear agreed to replace these amplifiers free of charge. Additionally, it would seem desirable to use the smallest resistance values possible for the summing circuit of figure (4.13). As it turns out, replacing each of the 1kΩ resistors with 100Ω resistors actually yielded poorer noise performance. It is yet to be determined if this is due to a fundamental limitation on the CLC425 design (perhaps due to the unusually small differential input impedance of 6kΩ) or a problem that is produced by out of specification CLC425 amplifiers.

To minimize the coupling of any extraneous noise into the detection circuitry several measures were taken. The transimpedance, summing, and differencing circuits were enclosed in metal boxes with the supply voltages passing through feedthroughs exterior to the metal enclosures. By-pass capacitors were placed at the outputs of the LM78/7905's (used to convert the ±15 Volt supplies used in the laboratory to the ±5 Volts needed to supply the CLC425's), at the biasing of the photodiodes, and at the inputs of the amplifiers. Finally, lead lengths were kept as short as possible and twisted pairs used where applicable.

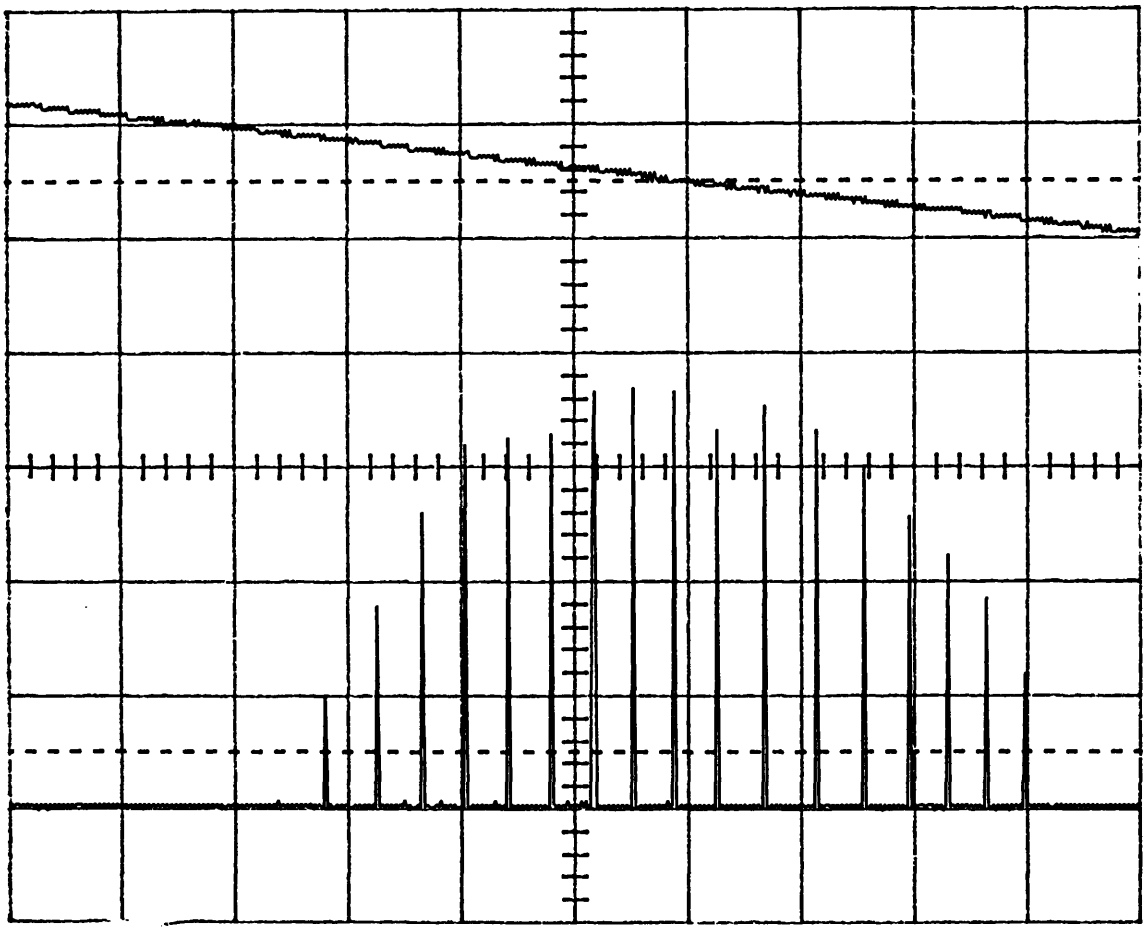

Figure 4.14: Trace of mode clusters from OPO. The top trace represents the PZT scanning waveform. The bottom trace is the mode cluster.

4.4 Feedback Stabilization of the Cavity

When the OPO is properly aligned and a triangle wave is applied to the PZTs, scanning the cavity length, a set of mode clusters appears as in figure (4.14). These mode clusters result when four conditions are met: conservation of energy, conservation of momentum, resonance of the signal, and resonance of the idler. For the measurement of intensity correlation it is necessary to lock the OPO cavity length to one of these resonances. In practice, it is virtually impossible to lock to the peak of a resonance; rather, the OPO is locked to the side of one of these peaks. This corresponds to a slight detuning of the signal and/or idler but, as explained in Chapter 3, this has minimal effect on the measured intensity correlation for the intended region of operation.

The feedback loop consists of four parts: the differencing circuit for the DC outputs of the two transimpedance amplifiers, a gain stage, a filter stage, and a high voltage/DC bias stage. The mechanical noise on the optical table is most prominent at frequencies in the audio range, with peak intensities around 400 Hz [17]. The filter was designed to address this problem. Essentially, it is has a 1/s response for high gains at low frequencies with rapid roll-off to ensure stability.

The 3-piece OPO, due to its excellent mechanical rigidity, is fairly stable under a steady-state voltage application to the PZT. Stable CW outputs can be achieved for 10-15 seconds without any feedback stabilization. The first cavity stabilized was a three-piece OPO with a cavity length of 38mm. The stability was for periods of over 20 minutes with robustness to a variety of acoustical disturbances. This cavity was stabilized with relative ease using the system of figure (4.15).

The idea is conceptually simple. The two signals from the signal and idler channels are subtracted in a differential amplifier (remembering that the outputs of the two channels are opposite in sign). A shunt capacitor appears across the non-inverting resistor to ground. This ensures that at frequencies above the several tens of kHz important for

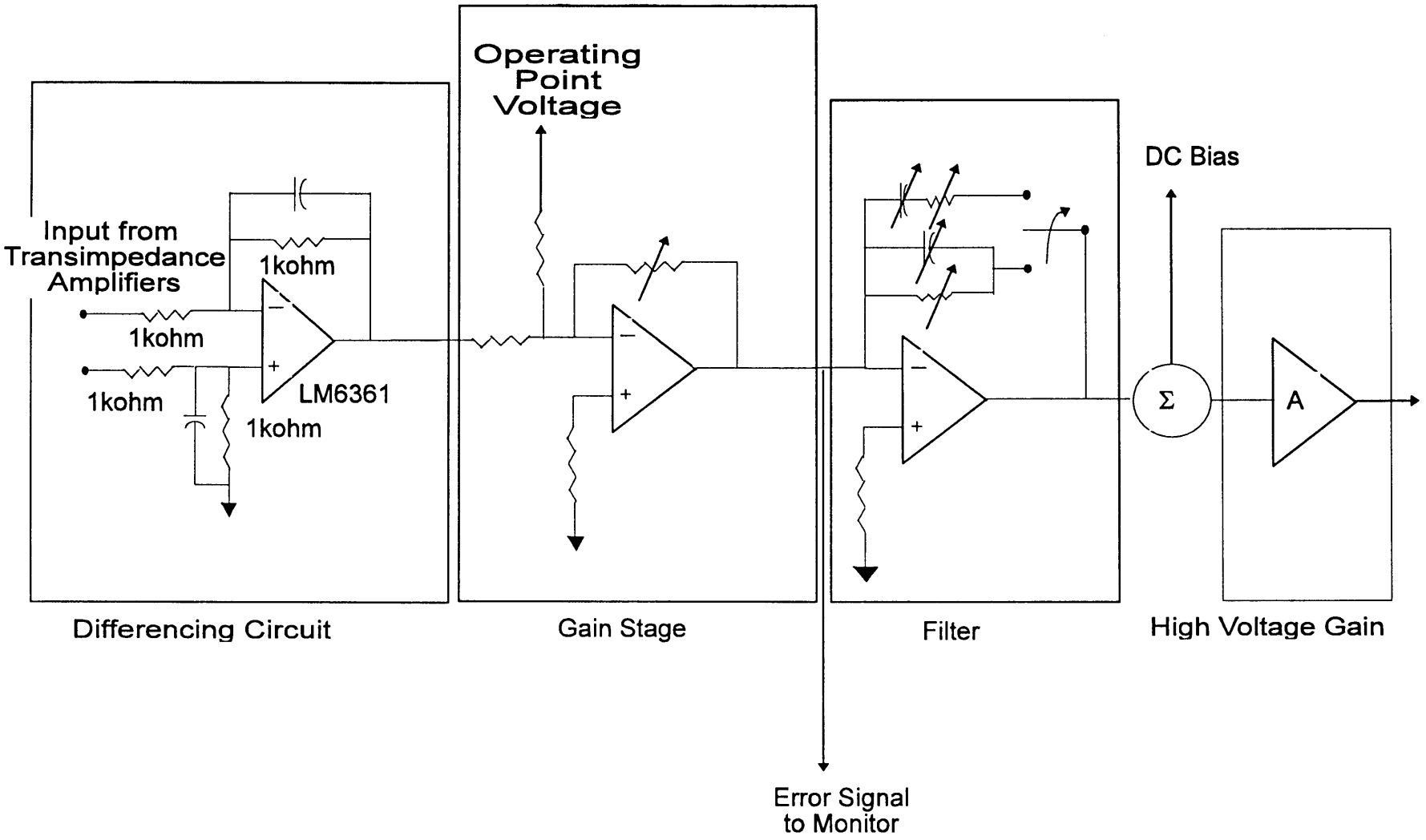

Figure 4.15: Cavity feedback stabilization circuit.

cavity locking the outputs of the CLC425's used in the transimpedance amplifiers see equal loads. It was experimentally established that at frequencies in excess of 10MHz the phase shift at the output of the CLC425 was strongly load dependent necessitating the latter mentioned consideration. The signal passes through the differencing stage and an inverting variable gain stage on to the aforementioned filter. The filter employs resistors and capacitors in series and parallel combinations with transfer functions of the form:

$$\frac{V_O}{V_I} = -\frac{sC_fR_f + 1}{sC_fR_i} \text{ (series RC)} \qquad (4.19)$$

$$\frac{V_O}{V_I} = -\frac{R_f}{R_i}\frac{1}{sR_fC_f + 1} \text{ (parallel RC)} \qquad (4.20)$$

where R_f and C_f are the feedback resistor and capacitor and R_i the input resistor to the filter stage.

The variability was implemented using a rotary switch allowing selection of several fixed values of R_f and C_f. Equation (4.19) is the implementation of a weighted integrator (roll-off at 20dB/decade) that flattens at $\omega = \frac{1}{C_fR_i}$, while equation (4.20) represents flat gain, then a roll-off (again at 20dB/decade) for frequencies greater than $\omega = \frac{1}{C_fR_f}$.

Not shown is a unity gain stage that can be manually switched between an inverting and non-inverting configuration. This allows locking to the leading or trailing edge of the gain peak. In practice, a thermal hysteresis induced asymmetry in the resonance peaks makes it much easier to lock to the leading edge.

The filtered signal is now summed with a DC voltage which establishes the operating point of the OPO. The summed signal is sent through a high voltage MOSFET gain stage to boost the output voltage to the levels needed to drive the PZT's.

A DC voltage is available at the input of the variable gain stage so that the OPO signal can be offset, bringing the mean output value of the variable gain stage to zero. Fluctuations about this mean constitute the error signal.

A MDT102 XYZ Flexure mount from Thor Labs was the first system used as a two-piece mount. Its commercial use is as a mount to align fiber optic cable but it has design features which make it desirable for use in the OPO set-up. The flexure design was originally thought to be more stable than other mounts that employed springs. Additionally, the mount allowed adjustment along the x-y-z axes (2mm in each direction) greatly facilitating the OPO alignment process. Two aluminum blocks were machined upon which were mounted the PZT-driven mirror and the crystal. These blocks were then epoxied to the MDT 102.

Considerable time and effort were expended trying to get this system to stabilize. Observing the output of the non-fedback OPO with a steady DC bias input showed that the design was inherently unstable (no CW OPO output could be achieved). The mount was placed on a rubber pad and realigned but this did not alleviate the fundamental instability of the mount. Several types of operational amplifiers were used in the gain and filter circuits, OP27 and HA2840 low noise amplifiers as well as LM6361 and LM6364 high speed amplifiers, in a variety of combinations, but with no success. At least part of the problem was traced to inadequate air pressure in the optical table, but this is not believed to be the primary reason for failure. Eventually this mount was abandoned.

The next type of mirror mount used was a Lee's LM4. This mount was of two piece design: a separable pedestal with overbored screw holes allowing coarse adjustability in the y-z plane (to which was attached the PZT/mirror), and a section housing the crystal that allowed angular adjustment about the y- and z-axes via spring loaded screws (the z-axis is taken normal to the optical table and the x-axis in the direction of beam propagation).

Under DC bias conditions, with no feedback, observation of the CW transmission of the OPO showed this mount to be superior to the Thor Lab's MDT 102, but still markedly inferior to the three-piece mount. Lock was, however, obtained using this mount. Figure (4.16) shows the error signal (centered vertically) and the offset voltage (~2.5 volts). The excursions from the mean are a sizable percentage of the lock point voltage. This stabilization is adequate, but marginally so, as lock can be easily lost to minor acoustical disturbance (i.e. ordinary speech).

4.5 THE CAVITIES

A monolithic cavity is the simplest possible design, having both input and output mirrors polished onto the crystal, and it requires no mechanical stabilization. Although compact and low loss, this configuration lacks flexibility in tuning and may suffer from thermal effects as well as having a reputation for being very difficult to align. These problems render this cavity intractable for practical use.

The three-piece cavity is highly flexible providing easy tuning and reasonably easy servo-locking. The primary disadvantage is the total round-trip loss (4 crystal interfaces per roundtrip). The three-piece cavity provides the benchmark for losses (worst of the three designs for a given crystal and output mirror) and degree of stability (best of the three).

The two-piece cavity strikes a good compromise between the one- and three-piece cavities. Cavity alignment flexibility is retained but the number of times the beam passes through crystal faces in one round trip is reduced from four (for the three-piece OPO) to two. Losses, due to reflection, are introduced with each passage through a crystal surface.

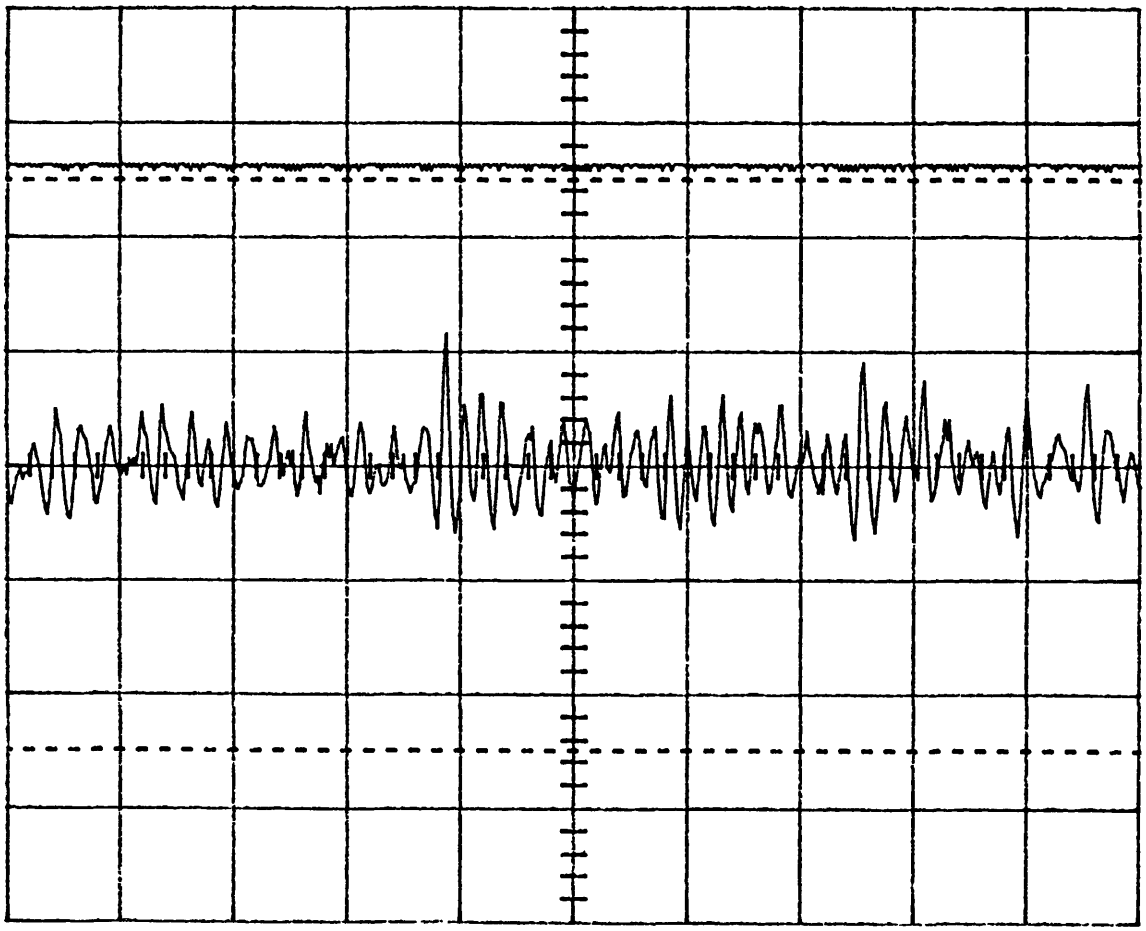

Figure 4.16: Error signal from the feedback loop for the two-piece OPO. The top trace is the offset operating point. The center trace represents the error signal. An ideal error signal would be flat and equal to zero. 5ms/div; 1Volt/div. The large fluctuations seen above 5MHz in figure (4.24) are attributable to this locking error.

This increases μ, thus decreasing the intensity correlation and increasing the amount of power required to achieve oscillation threshold. Accordingly, the two-piece OPO was the design of choice for the final experiment; nevertheless, the extremely high quality of the Airtron hydrothermally grown crystals and the REO input couplers together with the inherent stability of the three-piece cavity render the 3-piece design an attractive choice as well.

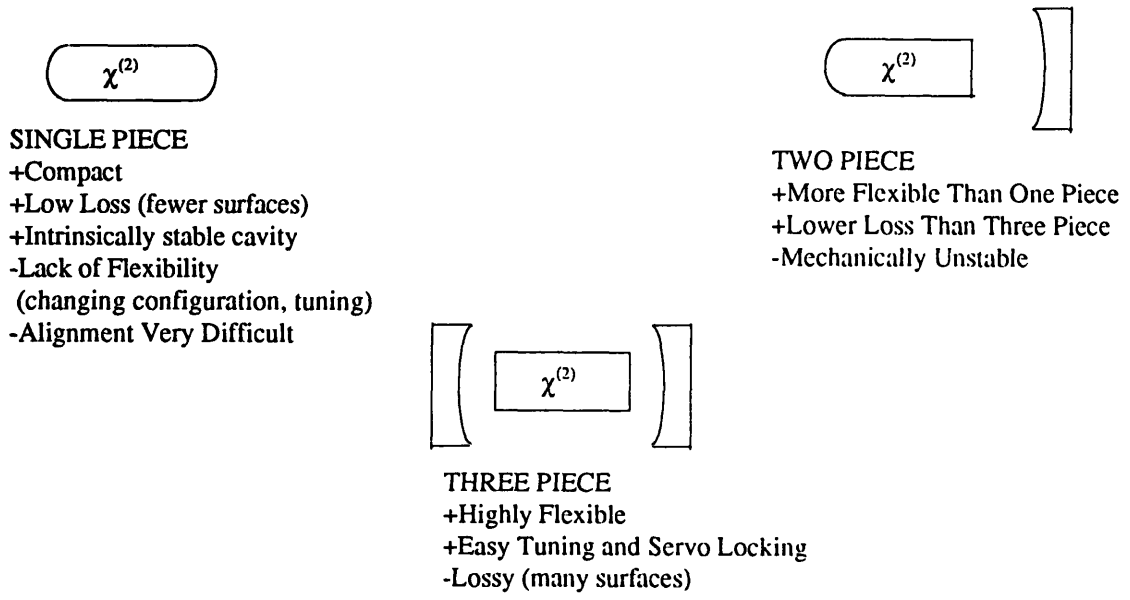

Figure 4.17: Cavity Designs.

As stated in the latter section a three-piece OPO of cavity length 38mm loaded with a 10mm long, Airtron grown and anti-reflection coated, crystal was pumped close to threshold and feedback stabilized. The cavity was formed by the first two mirrors listed in table (4.2). The threshold of this OPO was 30mW in good agreement with what could be predicted by other loss measurements. An earlier version of the detector system was available at this time. In this system only one of the two DC outputs from the photodetectors was used as the lock signal. The results proved to be rather poor. This cavity was disassembled and placed in a set-up being used to measure quantum phase-

noise. It was later realized the poor performance resulted from the loading effect on the transimpedance amplifier that drove the feedback circuit.

A new three-piece mount was machined. The base of the pedestal supported a New Focus 3902 4-axis mount for fine adjustments, on top of which was a hand-screw type turnstile rotational mount for coarse adjustment. The crystal was set on top of a machined aluminum block which was epoxied to the rotational mount. The physical length of the cavity, using the same mirrors as those given in the latter paragraph, is 14mm. The crystal used in this cavity was the Skytek/Thin Film Labs 28.13°-cut crystal of length 12mm.

A determined effort was made in trying to bring this OPO to threshold, but the efforts never came to fruition. The alignment procedure was hindered by the short cavity length but not enough to make alignment impossible. A finesse measurement was performed giving losses as per table (4.3). These losses seemed inordinately high, however, and eventually the crystal was put in a longer length cavity pumped by a Nd:Yag laser for second harmonic generation. As a result of these efforts it was finally determined that the crystal was improperly cut [22], explaining both the high losses and the failure to oscillate.

As given previously, the two-piece cavity was assembled from a Lee's LM4 mount, the IR T=.75% output coupler, and the 12mm long Skytek/Thin Film Labs crystal with a 40mm radius of curvature mirror polished (T=90.4% at 531nm and HR at 1.06μm) onto one end. The threshold was found to be 20mW after a lengthy tuning process. It appears as though a "sweet spot" exists on the crystal. At this point the threshold is about 2/3 what it is at other locations on the crystal. It is this OPO that was used in the final measurements given in the next section.

The same mount design was used with a 2.7% output coupler and was determined to have a threshold of 270mW. The threshold for this configuration, however, was never optimized, as will be explained in section 4.6.

4.6 Experimental Set-up

The pump source for the OPO is a Coherent Laser Kr^+-ion laser. It has a strong line at λ=531nm and provides 400mW of output power at 50A of plasma tube current up to 630mW at 65A of tube current. Due to the mechanical noise introduced through the cooling pump it is necessary to both intensity- and frequency-stabilize this pump laser. The intensity stabilization scheme looks as follows:

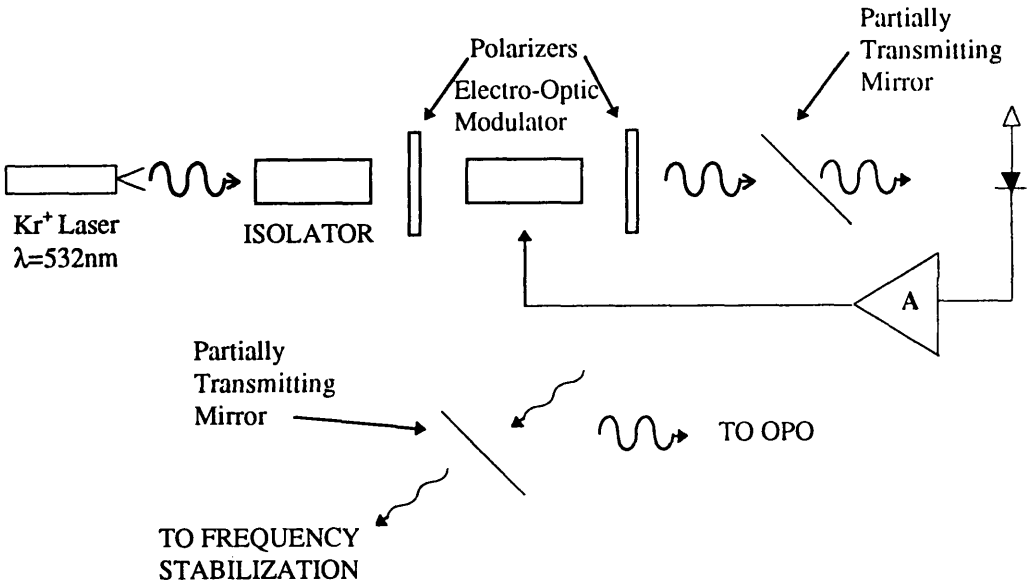

Figure 4.18: Intensity locking of the Kr^+ ion laser.

The Faraday isolator prevents feedback destabilization of the laser and has an extinction ratio of 10^5:1 [17]. The electro-optic modulator (EOM) causes rotation of the incident E-field polarization as a function of the applied voltage. The first polarizer passes only one sense of polarization. After passing through the EOM only the portion of the E-field that

projects onto the transmitting axis of the second polarizer is propagated. By changing the voltage applied to the EOM, and hence the amount of rotation of the E-field vector, the transmitted intensity may be controlled. The detection of a small amount of the transmitted radiation allows feedback stabilization of the operating point. With the laser thus intensity stabilized the intensity fluctuations fall from 7.5% p-p to less than .5% p-p.

The pump is frequency stabilized per the method of Drever, et. al. [23]. In this method a stable Fabry-Perot cavity, with a resonance at a frequency f_o equal to the desired pump frequency f_c, is used as a reference. A qualitative and approximate mathematical description of the stabilization scheme will be given.

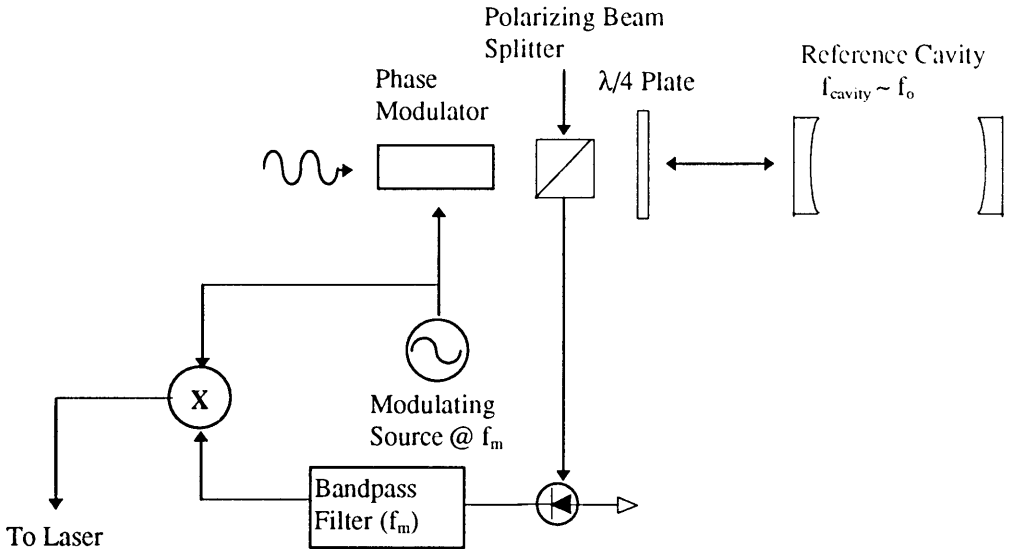

Figure 4.19: Frequency stabilization of the Kr^+ pump laser.

The beam passes through the phase modulator generating sidebands at $f_o \pm f_m$ (the higher order sidebands are too weak to be of concern). The beam, incident on the beam splitting polarizer, propagates through to the reference cavity. The two sidebands are far enough removed from the center frequency as to be totally reflected. The cavity, assumed to have standing waves at f_o, couples out a "leakage field".

The leakage field combines with the incident field that is assumed to be close enough in frequency to the cavity field to produce a reflection coefficient with a strong frequency dependent phase term. The polarization of the reflected signal also depends on the cavity resonance. It again passes through the wave plate returning to linear polarization, but orthogonally polarized to the pump field and is reflected at the beam splitting polarizer. The reflected field is received by a photodetector (recall that a photodiode is a square law detector). The result is band pass filtered and mixed with the modulating field (in essence, a heterodyne detection scheme). From the mixer emerges a phase sensitive DC term that drives the frequency. Thus locked, the pump laser linewidth is ~100 kHz [24].

Mathematically, the reflected signal is:

$$\text{Reflection} \approx e^{j\omega_o t}\left(Be^{j\phi(t)} + Ae^{j\omega_m t} - Ae^{-j\omega_m t}\right) \tag{4.21}$$

where A is determined by the depth of modulation, B is the magnitude of the sum of the incident and reflected signals, $\phi(t)$ is the frequency dependent phase term, and ω_m is the modulation frequency. Squaring equation (4.21) yields at the modulating frequency ω_m:

$$|\text{Reflection}|^2 = 4AB \sin\omega_m t \sin\phi(t) \tag{4.22}$$

After demodulation at $\sin\omega_m t$ and low-pass filtering:

$$\text{Output of Filter} = 4AB \sin\phi(t) \tag{4.23}$$

In the Drever FM locking technique $\phi(t)$ is a dispersive signal that is a function of the cavity resonance. At resonance $\phi(t) = 0$, $\phi(t) > 0$ for positive detuning, and $\phi(t) < 0$ for negative detuning. Hence the low-pass filter signal acts as an error signal and is used to lock the laser to the reference cavity.

In the experimental set-up the DC bias for the PZT stabilizing the reference cavity is manually scanned until strong transmission is seen, then the reference cavity is locked to the correct length also locking the frequency.

The experimental set-up to measure squeezing is shown in figure (4.20). The $\lambda/2$ plate at the output of the OPO allows the signal and idler to pass unhindered in one orientation, but when rotated 45° produces an even power split between the two channels for both the signal and idler beams. The latter configuration allows a convenient establishment of the shot noise level [4]. To verify this assertion, the shot noise as established by the latter method was compared to the shot noise produced in a white light illuminated single photodetector with a DC current equal to the sum of the individually illuminated diodes. White light is known to be a source of shot noise limited light [25]. The signal and idler beams were focused onto the photodetectors with the incident beam waist being 1/6 the diameter of the photodetector active area.

The common mode rejection of the detection circuit was established by injecting a reference signal at 5MHz into the intensity feedback loop using a function generator. Figure (4.21a) shows the signal as it appears in one photodetector with 3mA of photocurrent. Figure (4.21b) shows the injected signal with 1.5mA in each channel. This is the worst case measurement (-29dBm) over the frequency range 1-5MHz and with a poor quality lock (prior to the discovery of inadequate air pressure floating the optical table). Typically, the rejection was in excess of -30dBm with results as high as -34dBm.

Figures (4.22) shows the electronic noise floor of the detector system (the output of the summing amplifier is boosted by 22dBm with a Hewlett-Packard amplifier model 8447E). Note the rapidly rising noise floor beyond 5MHz. At frequencies below 2MHz the 1/f noise of the spectrum analyzer is dominant. Figures (4.23) show the output of each detector with 1.5mA of photocurrent. Note that the noise spectrum is well above the shot noise expected for this amount of current. The excess is caused by technical noise in the pump.

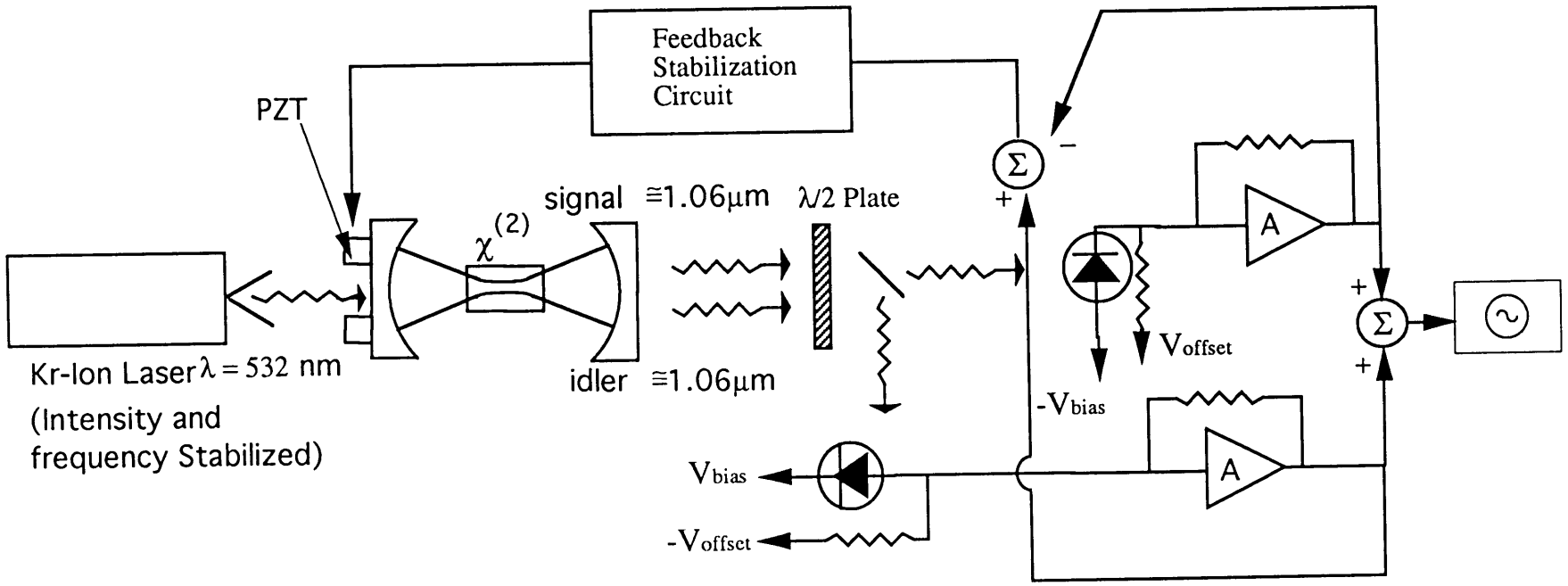

Figure 4.19 Final experimental set-up

Figure (4.24) shows the noise floor for the Tektronix 496P Spectrum analyzer and the Hewlett-Packard model 8447E amplifier. The 1/f noise is prominent out to about 10MHz then the noise flattens. The roll-off is rapid enough that measurements are affected only in the range ~ 0-2.5MHz.

4.7 Measurements

One photodetector was measured to be 1.2% more efficient than the other. As explained in Chapter 3, this results in incomplete cancellation of the technical noise. To compensate for this a variable resistor was added to the input of the transimpedance amplifier of the most efficient device to attenuate the additional signal. Approximately 8Ω was used for the compensation.

No attempt was made to bring the signal and idler to degeneracy. Rather the system losses were minimized (thereby maximizing intensity correlation) by tuning the pump input angle and location until the lowest oscillation threshold was found. The actual operating point must be within 10nm of wavelength degeneracy because that is the angle tuning range of the 3X3X12 crystal.

Figure (4.25a) shows the white light generated shot noise floor for a single diode illuminated so as to produce 3mA photocurrent while figure (4.25b) shows the intensity correlation measured for this system. Study of the plot of the shot noise spectrum and of the correlated spectrum shows that the noise of the correlated spectrum increases much more rapidly than the shot noise spectrum below 2 MHz. For the case of the shot noise (which is ideally flat) the rise is attributed to the additional noise contributed from the 1/f noise of the spectrum analyzer. The spectrum of the differenced signal-idler outputs rises both due to the 1/f noise and incomplete cancellation of pump noise. This is due to an imbalance in the losses of the two channels. The rapid fluctuations of the noise at

frequencies above 5MHz are attributable to the marginal cavity stabilization lock. The OPO was operated at 1.5 times threshold.

Subtracting off the contribution of the electronic/spectrum analyzer noise at 3MHz from both the shot noise and correlated noise, a reduction of 2.1dBm is observed; or equivalently 38.3% intensity correlation. The cavity linewidth of this cavity is approximately 10MHz. From the information given in Chapter 3 one expects best correlation to occur at 1 or 2MHz; exactly where the excess noise is most prominent. Therefore, it is likely that the point of best correlation is not being seen for this system.

As stated in table (4.3) the losses for this cavity as predicted by the finesse measurement seem overly optimistic. Using the measured data for reflection losses (averaging the two polarizations), absorption losses (again averaging the two polarizations), mirror losses and transmission coefficient (the loss of the mirror polished onto the crystal surface has never been measured and will be assumed to be equal in loss to the other Airtron mirrors), an assumed detector quantum efficiency of .90, a measured beam-splitter efficiency of .99, and a measured transmission quantum efficiency through the $\lambda/2$ plate and polarizing beam splitter of .98 the expected maximum squeezing is:

$$(S_{DET})_{max} = 1 - \left(\frac{.75}{.75 + 2(.035+.06)+.11+.05}\right)(.9)(.99)(.98) = .542$$

or in dB:

$$(S_{DET})_{max} = 10\log.542 = -2.66\text{dBm}$$

which when compared to the measured reduction of -2.1dBm seems reasonable, as stated earlier, since the point of best correlation is probably not being observed.

The .75% output coupler of this cavity was replaced by an REO 2.7% output coupler. Since the larger output coupler reduces the finesse of the cavity, and the cavity linewidth is given as $\frac{2\tilde{\phi}}{\text{Finesse}}$, the linewidth for this cavity is ≈ 50MHz. Hence, not only is better correlation expected, the frequency at which best correlation occurs should appear at a frequency higher than those affected by the pump noise and spectrum analyzer 1/f noise.

There is considerable propogation loss through the isolator and EOM in the pump system, so that even at 65A of tube current only about 350mW reached the input coupler of the OPO. The estimated threshold for this cavity was on the order of 270mW. Normally, the initial alignment procedure requires at least 1.5 times this amount to get the OPO oscillating (then the alignment is tuned to optimal). In order to optimize the power incident on the OPO the EOM was removed and the OPO brought to threshold and coarsely optimized to approximately 270mW.

The EOM was then replaced, which necessitates further alignment to re-establish the threshold condition. A problem surfaced with the pump laser at this point; the Kr^+ plasma tube overpressurized with a resultant loss of power. This condition required attention from a qualified service technician. Thus the intensity correlation of this system could not be measured prior to the completion deadline of this work.

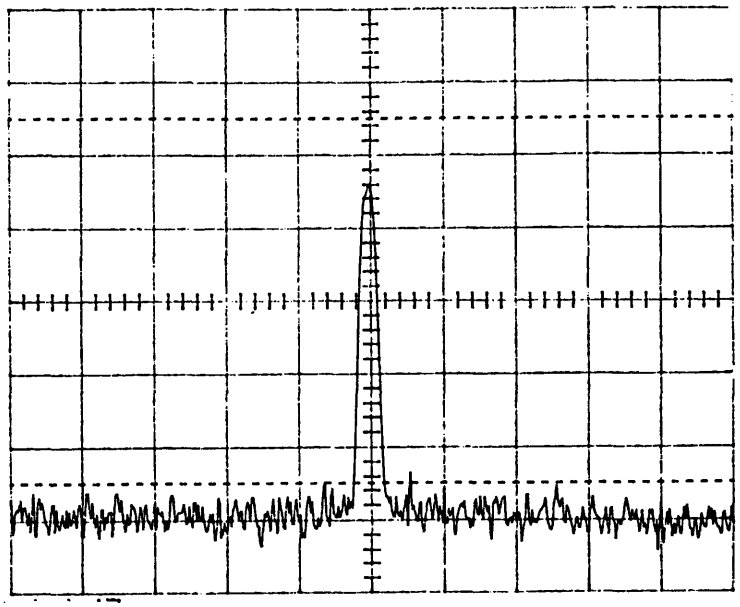

Figure 4.21a

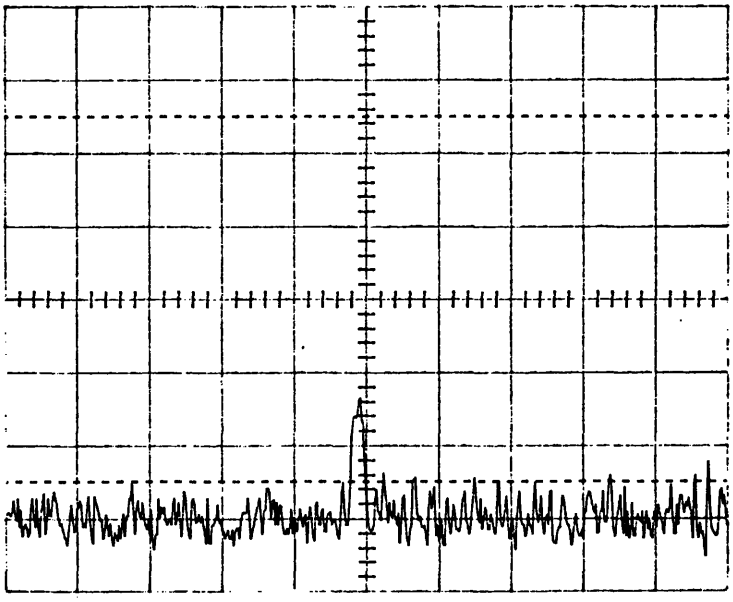

Figure 4.21b

Figure 4.21: a) The output of a single photodetector/transimpedance amplifier illuminated to produce 3mA of photocurrent. The sharp center spike is injected through the intensity lock. b) The output of the sum of both photodetector/transimpedance amplifiers each illuminated to produce 1.5mA. 50 kHz/div; 5MHz center frequency; 10dB/div; 10 kHz resolution bandwidth. 29dBm of common mode suppression is obtained.

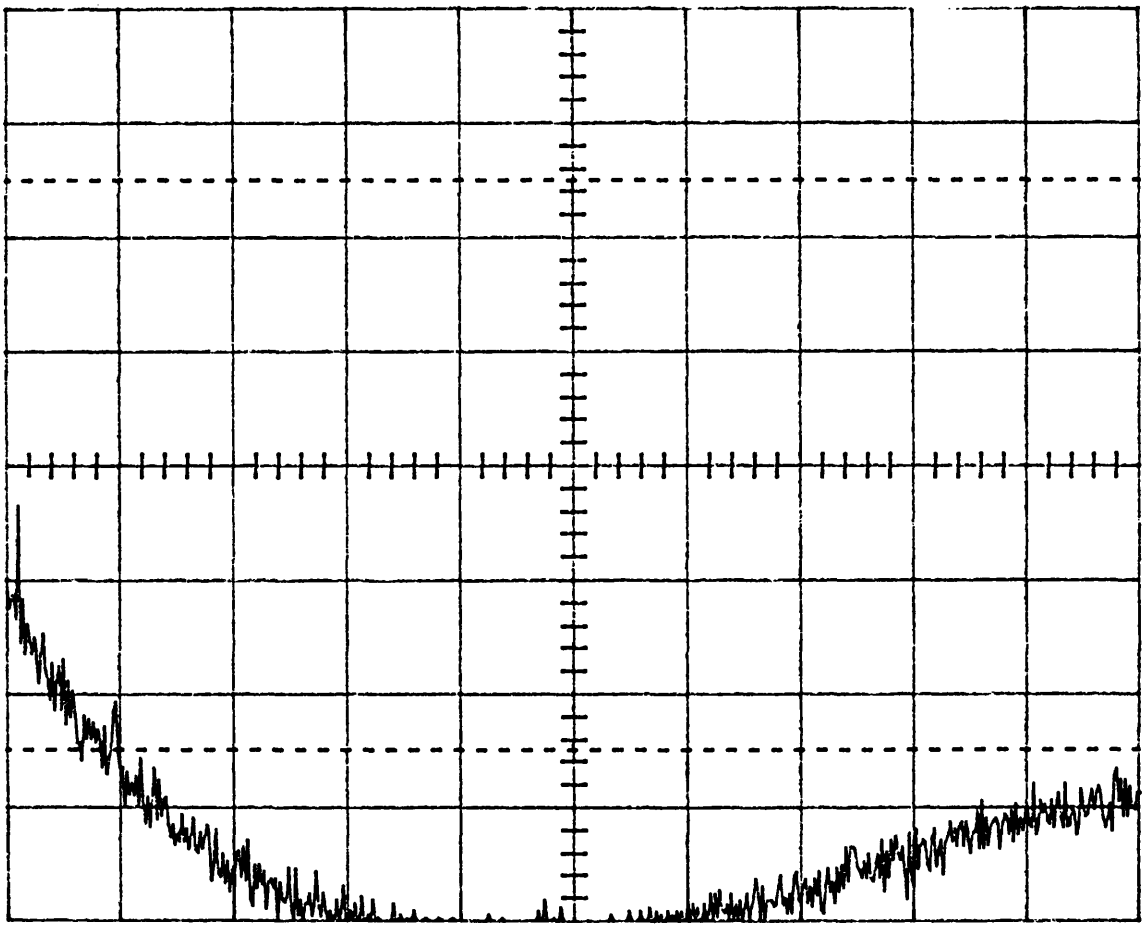

Figure 4.22: The electronic noise floor of the two photodetectors plus the summing amplifier. The large low frequency noise results from the 1/f noise of the spectrum analyzer while the rising floor at higher frequencies results from the diode capacitance. 1 MHz /div; 0-10 MHz; 2dBm/div; 100 kHz RBW; top grid represents -85dBm.

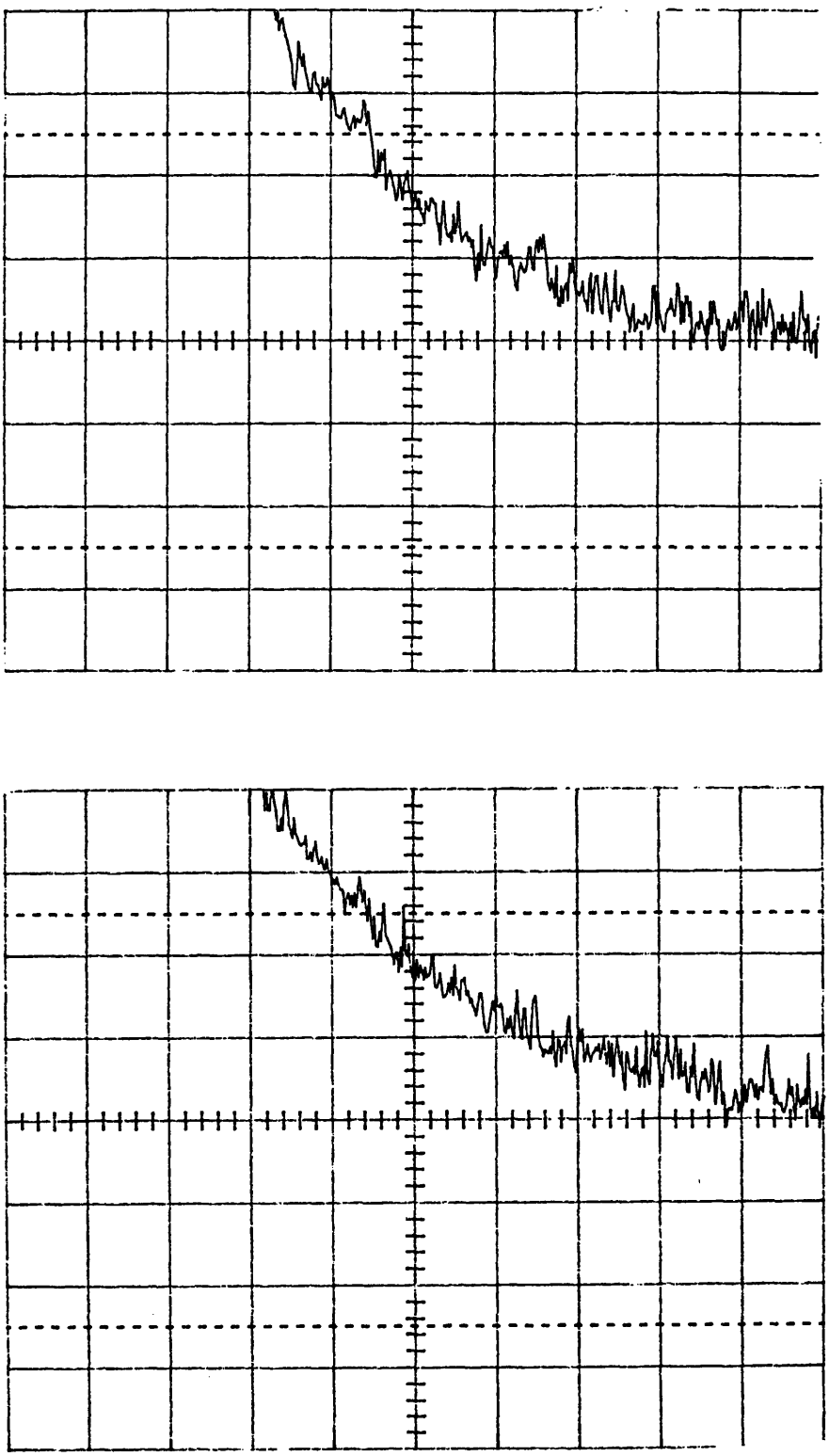

Figure 4.23: Single channels, each with 3mA of OPO produced photocurrent. 1 MHz/div 0-10 MHz; 10dBm/div; 100 kHz RBW; top grid represents -85dBm.

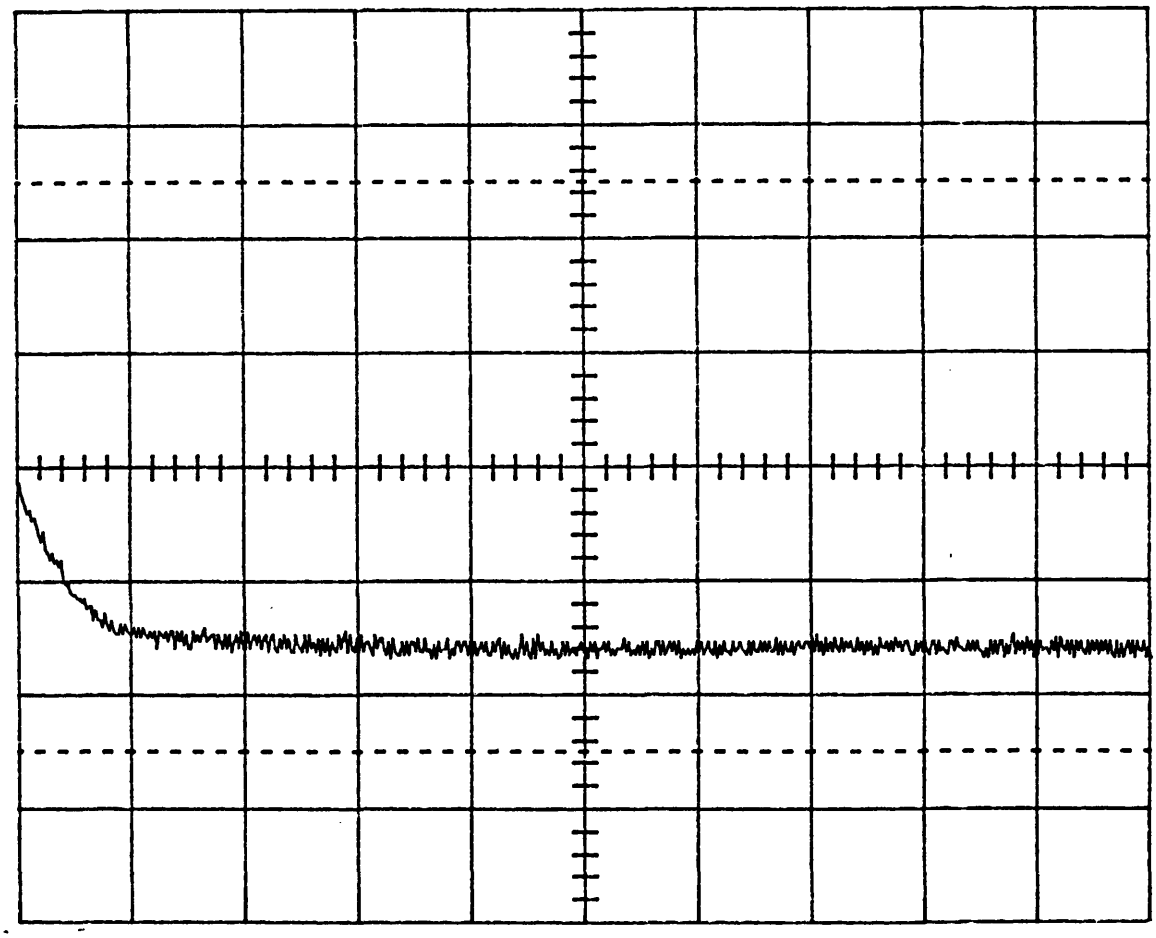

Figure 4.24: Spectrum analyzer noise of Tektronix 496P Spectrum analyzer and Hewlett-Packard Model 8447E +22dBm amplifier. 10MHz/div; 0-100MHz; 100kHz RBW; 2dBm/div. The center line represents -80dBm.

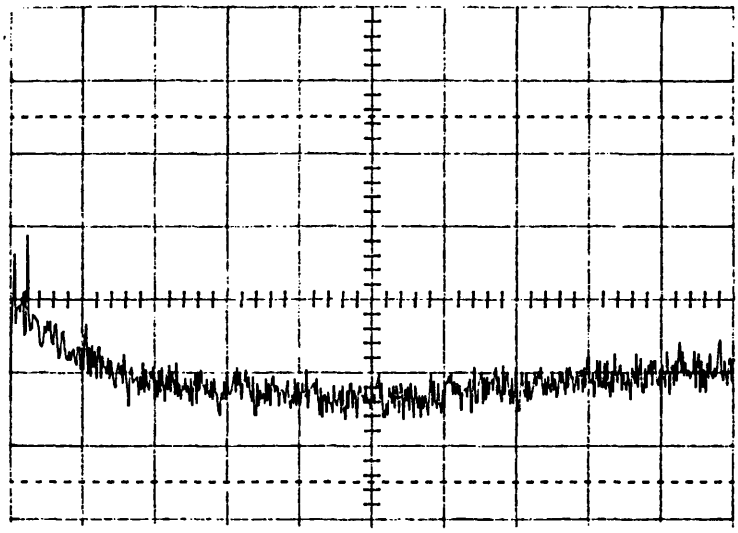

Figure 4.25a

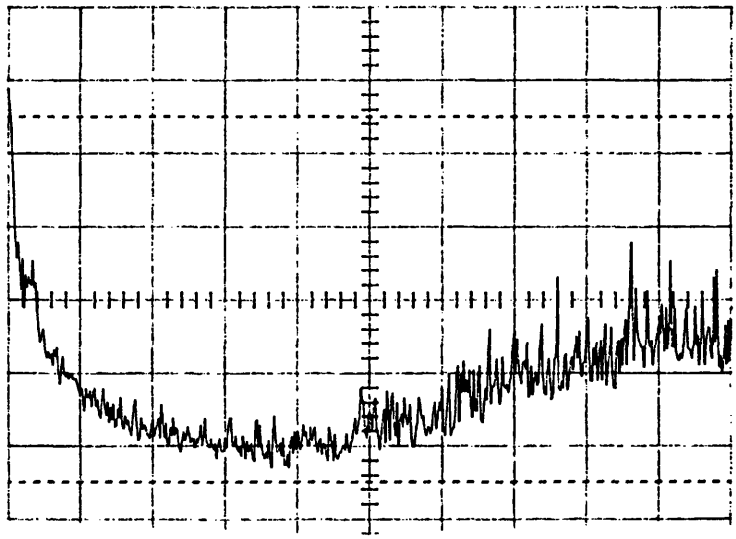

Figure 4.25b

Figure 4.25: a) Shot noise floor for 3mA of white light generated photocurrent in a single detector. The low frequency rise is due to spectrum analyzer 1/f noise while the higher frequency noise results from an increasing electronic noise floor. b) The intensity correlated spectrum for the sum of the outputs of the two photodetectors illuminated by the signal and idler channels of the OPO with 1.5mA of photocurrent/channel. The correlation (corrected for electronic noise) at 3MHz is 2.1dBm. 1MHz/div; 0-10MHz; 2dBm/div; 100kHz RBW; top grid represents -85dBm.

CHAPTER 5

CONCLUSION

5.1 Summary

A two-piece optical parametric oscillator (with .75% output coupling) was characterized, designed, tested and used to generate intensity correlated light. The photodetection circuit has a bandwidth of over 40MHz and has demonstrated linearity for 3mA of white light generated photocurrent. This system was used to generate squeezing of -2.1dBm at 3MHz. A similar system with a 2.7% output coupler was also built and brought to threshold but technical difficulties prevented measurement of intensity correlation.

A three-piece cavity system was also characterized, designed, and brought to threshold but was disassembled for use in another experimental set-up before a correlation measurement could be made.

5.2 Future Work

The obvious first step in continuing the work presented here is to measure the intensity correlation produced by the two-piece OPO with the 2.7% output coupler. It is expected this system will generate in excess of 80% intensity correlation. Also, the two

replacement CLC425s provided by Comlinear must be substituted for the out of (noise) specification devices presently installed in the transimpedance amplifiers. This should reduce the noise floor by 2dBm.

The very high quality of the REO mirrors and the superior anti-reflection coatings on the Airtron crystal still make the three-piece OPO a viable alternative to the two-piece system; especially when one considers the inherent mechanical stability of the three-piece cavity. It would be worthwhile to compare the intensity correlation produced by the three-piece cavity to the two-piece cavity. From the loss measurements made, it seems likely they would provide similar maximum correlation. This would also permit quantification of the effect on the output spectrum of the marginal two-piece cavity lock.

In line with these comments, time must be devoted to perfecting the feedback stabilization of the two-piece cavity. Better characterization of the system is indicated. A number of possible solutions warrant consideration. These include improving the filter, better mechanical isolation of the cavity, characterization of the PZT, and improving the rigidity of the two-piece design.

Although the CLC425 is inexpensive, superior amplifier noise performance may be garnered from hybrid MOSFET-BJT devices (albeit at a significant price increase). The low frequency electronic noise is still dominated by the thermal noise of the feedback resistor. An enticing possibility, although probably fraught with difficulties, is to use a low noise FET device in the feedback path in place of the resistor. This would also permit simple adjustments in the amount of feedback by adjusting the bias of the feedback FET.

The junction capacitance of the photodiode presents a problem and a possible compromise may be afforded by the Epitaxx500T (active diameter of .5mm). It offers the same power limit (100mW) as the Epitaxx1000T (albeit with an increased likelihood of local saturation) but with approximately 1/4 the capacitance. Such a substitution would

increase the bandwidth and dynamic range at the price of a small reduction in power handling capabilities.

Once these problems have been solved a wide variety of quantum noise phenomena may be studied. One such possibility is an injection-seeded optical parametric amplifier operating in the saturated gain regime [26]. Many other possibilities exist when one considers the wide range of operating regimes of the OPA/OPO.

Bibliography

[1] A. Heidman, R. J. Horowicz, S. Reynaud, E. Giacobino, and C.Fabre, "Observation of Quantum Noise Reduction on Twin Laser Beams," Physical Review Letters, Volume 59, Number 22, 30 November 1987, pp.2555-2557.

[2] Special Issue on "Squeezed States of the Electromagnetic Field," Journal of the Optical Society of America, Volume B4, Number10, October 1987.

[3] J. Mertz, A. Heidman, C.Fabre, E. Giacobino, and S. Reynaud, "Observation of High-Intensity Sub-Poissonian Light Using an Optical Parametric Oscillator," Physical Review Letters, Volume 64, Number 24, 11 June 1990, pp. 2987-2990.

[4] J. Mertz, T. Debuisschert, A. Heidman, C.Fabre, and E. Giacobino, "Improvements in the observed intensity correlation of optical parametric oscillator twin beams," Optics Letters, Volume 16, Number 16, 15 August 1991, pp. 1234-1236.

[5] K.W. Leong, N.C. Wong, and J.H. Shapiro, "Nonclassical intensity correlation from a type I phase-matched optical parametric oscillator," Optics Letters, Volume 15, Number 19, 1 October 1990, pp.1058-1060.

[6] R. Graham and H. Haken, "The Quantum Fluctuations of the Optical Parametric Oscillator. I," Z. Physik, Volume 210, 1968, pp. 276-302.

[7] R. Loudon, The Quantum Theory of Light, Second Edition, Clarendon Press, Oxford, 1983.

[8] Amnon Yariv, Quantum Electronics, Third Edition, John Wiley and Sons, New York 1989.

[9] Amnon Yariv, Optical Electronics, Fourth Edition, Holt, Rinehart and Winston, Inc., 1991.

[10] Hermann A. Haus, Waves and Fields in Optoelectronics, Prentice-Hall, Inc. New Jersey, 1984.

[11] E.P. Ippen, "Nonlinear Optics," Lecture Notes, MIT Subject 6.634, Spring 1994.

[12] Dr. N.C. Wong (private communication)

[13] J.E. Bjorkholm, A. Ashkin, and R.G. Smith, "Improvement of Optical Parametric oscillators by Nonresonant Pump Reflection," IEEE Journal of Quantum Electronics, QE-6, December 1970, pp. 797-799.

[14] G.D. Boyd and D.A. Kleinman, "Parametric Interaction of Focused Gaussian Light Beams," Journal of Applied Physics, Volume 39, Number 8, July 1968, pp.3597-3639.

[15] J.L. Nightingale, "Fundamental Walk-off Compensation in KTP," Company Memo Coherent Laser Group, 1 June 1993.

[16] K.W. Leong, N.C. Wong, and J.H. Shapiro, "Quantum Correlation and absorption spectroscopy in an optical parametric oscillator in the presence of pump noise," Optics Letters, Volume 15, Number 16, 15 August 1990, pp.891-893.

[17] Kin Wai Leong, "Intensity Quantum Noise Reduction With An Above-Threshold Optical Parametric Oscillator," Ph.D. Thesis, Massachusetts Institute of Technology, February 1991.

[18] Kong, J.A., Electromagnetic Wave Theory, Second Edition, John Wiley and Sons, Inc., 1990.

[19] C. Fabre, E. Giacobino, A. Heidman, S. Reynaud, "Noise Characteristics of a Non-Degenerate Optical Parametric Oscillator-Application to Quantum Noise Reduction," Journal of Physics (France), Number 50, 15 May 1989, pp. 1209-1225.

[20] C. W. Gardiner, Quantum Noise, Springer-Verlag, Berlin, 1991.

[21] Applications Note, Casix.

[22] E. Mason (private communication)

[23] R.W.P. Drever, J.L. Hall, F.V. Kowalski, J. Hough, G.M. Ford, A.J. Munley, and H. Ward, "Laser Phase and Frequency Stabilization Using an Optical Resonator," Applied Physics B, 31, 1983, pp. 97-105.

[24] D. Lee (private communication)

[25] R.S. Kennedy, "Communication through Optical Scattering Channels: An Introduction," Proceedings IEEE, Volume 58, 1970, pg. 1651.

[26] N.C. Wong, "Squeezed Amplification in a Nondegenerate Parametric Amplifier," Optics Letters, volume 16, Number 21, 1 November 1991, pp.1698-1700.